

The effects of phosphorus pentoxide additions on the thermal, rheological and structural properties of sodium borosilicate glass

LOVE, Katrina, GEORGE, Jamie, BELL, Anthony, SWEENEY, Francis, CUTFORTH, Derek, LONERGAN, Charmaine, DIXON, Derek, KRUGER, Albert and BINGHAM, Paul <<http://orcid.org/0000-0001-6017-0798>>

Available from Sheffield Hallam University Research Archive (SHURA) at:

<https://shura.shu.ac.uk/30955/>

This document is the Published Version [VoR]

Citation:

LOVE, Katrina, GEORGE, Jamie, BELL, Anthony, SWEENEY, Francis, CUTFORTH, Derek, LONERGAN, Charmaine, DIXON, Derek, KRUGER, Albert and BINGHAM, Paul (2023). The effects of phosphorus pentoxide additions on the thermal, rheological and structural properties of sodium borosilicate glass. *Journal of Non-Crystalline Solids*, 600: 121999. [Article]

Copyright and re-use policy

See <http://shura.shu.ac.uk/information.html>



The effects of phosphorus pentoxide additions on the thermal, rheological, and structural properties of sodium borosilicate glass

K.L. Skerratt-Love^a, J.L. George^b, A.M.T. Bell^a, F. Sweeney^a, D. Cutforth^b, C.E. Lonergan^b, D.R. Dixon^b, A.A. Kruger^c, P.A. Bingham^{a,*}

^a Materials and Engineering Research Institute, Sheffield Hallam University, City Campus, Sheffield, S1 1WB South Yorkshire, UK

^b Pacific Northwest National Laboratory, PO Box 999, Richland, 99352 WA, USA

^c Office of River Protection, 2440 Stevens Center Pl, Richland, 99354 WA, USA

ARTICLE INFO

Keywords:

Phosphate
Borosilicate
Phase separation
Glass
Waste

ABSTRACT

This research has characterized the effects of P₂O₅ additions on the physical, chemical, thermal, rheological properties and the structure of SiO₂-B₂O₃-Na₂O glasses relevant to radioactive waste immobilization. Properties analysed include high-temperature viscosity, glass transition temperature (T_g) and structure. X-ray diffraction (XRD) confirmed a solubility limit of between 3.0 and 4.0 mol% P₂O₅ for the onset of crystallinity with formation of Na₃PO₄ and Na₄P₂O₇ in annealed bulk glasses; and between 4.0 and 5.0 mol% P₂O₅ in unannealed (quenched) glasses. This difference in behaviour is attributed to the bulk glass annealing temperature being greater than T_g of phase-separated, phosphate-rich droplet phases present in the 4.0 mol% P₂O₅ glass, which promoted crystallization, where back scattered scanning electron microscopy (SEM) images suggested that phase separation had occurred as liquid-liquid phase separation, where there was evidence of a droplet like morphology in glasses containing between 4.0 and 6.0 molar % P₂O₅. However, the exact mechanism cannot be unequivocally confirmed as nucleation and growth based purely on phase morphology. Differential Thermal Analysis (DTA) and dilatometry showed modest increases in T_g with increasing P₂O₅ contents below the onset of crystallisation and a more substantial increase coinciding with the onset of crystallisation between 3.0 and 4.0 mol% P₂O₅. High-temperature viscosity measurements showed that increasing P₂O₅ contents led to increases in viscosity, with samples containing the highest P₂O₅ additions displaying non-Newtonian behaviour consistent with the presence of crystals in the melt at 950 °C. Raman difference spectra showed that the increase in P₂O₅ content resulted in characteristic peak intensities at 729 cm⁻¹, 937 cm⁻¹, 1000 cm⁻¹, 1026 cm⁻¹, 1109 cm⁻¹ and 1445 cm⁻¹ which were associated with phosphate species.

1. Introduction

The Hanford Site in Washington State currently hosts ~56 million gallons of radioactive waste stored in 177 underground steel tanks [1,2]. The waste consists primarily of first cycle discharges from the reprocessing of spent nuclear fuels. The high-level activity waste (HLW), when subjected to a pre-treatment regime, allows for the separation of the low-level activity waste (LAW) fraction. In the LAW and HLW waste treatment plant (WTP) facilities, the wastes will be mixed with glass-forming additives and vitrified to form borosilicate glasses [2]. The current strategy involves the near-term startup of a direct-feed LAW vitrification process planned to vitrify the first 10 M gallons of LAW.

Phosphorus pentoxide (P₂O₅) is present in some Hanford site defence

radioactive wastes that are to be converted into vitrified waste forms based on alkali borosilicate glass systems [1,5,6]. The P₂O₅ in the wastes originates from the Bismuth Phosphate, Reduction and Oxidation (REDOX) and Plutonium Uranium Reduction Extraction (PUREX) processes that were used for plutonium extraction from irradiated uranium [7]. P₂O₅ can be problematic because it is poorly soluble in alkali borosilicate glass systems, with concentrations greater than ~3 mol% or ~4.5 wt% [10,11] leading to phase separation which can affect melt viscosity and chemical durability [3,4,12–14]. In some Hanford waste glasses, P₂O₅ will be present at levels that may impact on melter performance and wasteform properties [13,25]. Phase separation can be undesirable because it can lead to formation of phases possessing different chemical and mechanical properties, which may increase the

* Corresponding author.

E-mail address: p.a.bingham@shu.ac.uk (P.A. Bingham).

<https://doi.org/10.1016/j.jnoncrysol.2022.121999>

Received 6 May 2022; Received in revised form 15 September 2022; Accepted 26 October 2022

Available online 15 November 2022

0022-3093/© 2022 The Authors. Published by Elsevier B.V. This is an open access article under the CC BY license (<http://creativecommons.org/licenses/by/4.0/>).

leachability of radionuclides present in the wastefrom, and hence reduce the integrity of the wastefrom. The $\text{Na}_2\text{O-B}_2\text{O}_3\text{-SiO}_2$ glass system could be considered to comprise three binary systems ($\text{B}_2\text{O}_3\text{-SiO}_2$, $\text{Na}_2\text{O-B}_2\text{O}_3$, and $\text{Na}_2\text{O-SiO}_2$) which are each prone to immiscibility, and where the ternary system $\text{Na}_2\text{O-B}_2\text{O}_3\text{-SiO}_2$ exhibits an immiscibility dome [15]. Heat treatments of melts in this system serve only to alter the structural characteristics of the separated phases present [15]. If the quenched glass is heat treated above its T_g , this initiates phase separation where spherical droplets enriched in B_2O_3 are dispersed in a matrix enriched in SiO_2 , where this metastable phase separation is referred to as either glass-glass or amorphous-amorphous phase separation [16]. The glasses described herein do not have compositions that lie within the $\text{Na}_2\text{O-B}_2\text{O}_3\text{-SiO}_2$ immiscibility dome, with the base (mol%) composition of 27.91 Na_2O -16.28 B_2O_3 -55.81 SiO_2 . This means that without the additions of P_2O_5 , this glass should not exhibit phase separation, even when heat treated.

The Hanford site wastes are complex mixtures of components and understanding the singular effects of P_2O_5 in these glass systems is challenging. Hence, simplification of the system has been undertaken here to understand the effects of P_2O_5 on glasses in the $\text{SiO}_2\text{-B}_2\text{O}_3\text{-Na}_2\text{O}$ system.

The aim of this study is to characterise the effects of P_2O_5 on physical, chemical, thermal, rheological properties and the structure of $\text{SiO}_2\text{-B}_2\text{O}_3\text{-Na}_2\text{O}$ glasses, i.e., high-temperature viscosity, glass transition temperature (T_g) and structure. The sodium borosilicate glass composition used in the present study is a simplification of a select series of Hanford radioactive glasses based on HLW and LAW, as the original compositions were far too complicated, with many components, to enable detailed structural analysis, for example by Raman spectroscopy. The HLW compositions were based on PNNL and ORP glass systems and were taken from the report 245590-HLW-RPT-05-001 [17]. The LAW compositions were based on WTP-LAW taken from the reports VSL-01R3560-2 [18] and VSL-03R3460-1 [19], and from the Office of River Protection (ORP)-LAW compositions taken from the reports VSL-04R4960-1 [20], VSL-05R5900-1 [21], VSL-06R6900-1 [22], VSL-07R1130-1 [23], VSL-09R1510-2 [24], VSL-10R1790-1 [25]. The glass series studied, sodium borosilicate doped with P_2O_5 (NBSP) has a constant molar ratio between $\text{Na}_2\text{O}:\text{B}_2\text{O}_3:\text{SiO}_2$ with varying P_2O_5 content. Glasses were characterised in order to determine the effects of P_2O_5 on the compositional, thermal, rheological, physio-chemical, and structural properties.

In alkali and alkaline earth silicate glasses, phosphate units do not fully incorporate into the silicate network, but instead form phosphate-rich regions with low degrees of connectivity, in orthophosphate (PO_4^{3-}) and pyrophosphate ($\text{P}_2\text{O}_7^{4-}$) units, which are then charge-compensated by sodium cations from the silicate sub-network [25–30]. In an alkali borosilicate glass system, P_2O_5 appears as ortho- and pyrophosphates, where the latter has been observed to bond to borate units through P-O-B linkages [27,31–33]. The incorporation of increasing concentrations of P_2O_5 in this manner leads to an increase in the ratio of 3-coordinated boron ($^{[3]}\text{B}^{3+}$) to 4-coordinated boron ($^{[4]}\text{B}^{3+}$), i.e. the $^{[3]}\text{B}^{3+}:\text{B}^{3+}$ ratio, accompanied by an increase in the degree of polymerization of the silicate network [31,34,35] where increasing P_2O_5 content saw a decrease in the abundance of Q_3^3 units and increase in the abundance of Q_4^3 units (re-polymerisation) [31–33]. Krishnamurthy et al. [31] and Stone-Weiss et al. [35] suggested the P_2O_5 was charge-compensated by Na^+ ions from the silicate sub-network and not the borate sub-network [31]. When P_2O_5 is introduced into the sodium borosilicate glass system, some of the sodium ions preferentially associate with non-bridging oxygens (NBOs) of the phosphate tetrahedra [31,34,35] depleting the borosilicate network of charge-balancing cations [31,34,35].

Polymerisation of the silicate and borate sub-networks refers to the distribution of Q^n units, which is indicative of the degree of polymerisation. SiO_2 consists of corner-sharing SiO_4 tetrahedra with bridging oxygens (BOs) linked to neighbouring SiO_4 tetrahedra, where the

additions of alkali or alkaline earth cations acting as network modifiers result in the formation of NBOs via the breaking of linkages between SiO_4 tetrahedra [36]. The mechanism of polymerisation of the network can be written as $2\text{SiO}^- \rightleftharpoons \text{Si-O-Si} + \text{O}^{2-}$ [27]. B_2O_3 consists of corner-sharing BO_3 triangles, of which a proportion are combined together to form three-membered boroxol ring units [36]. When alkali or alkaline earth cations acting as network modifiers are added, two possible outcomes arise: (i) the creation of a NBO which destroys the link between two trigonally-coordinated $^{[3]}\text{B}^{3+}$ units; or (ii) the conversion of $^{[3]}\text{B}^{3+}$ to $^{[4]}\text{B}^{3+}$ without the formation of a NBO [36].

In borate and silicate glass systems the extent of miscibility gaps can be influenced by network modifiers and is related to their polarising power [37,44]. Polarising power is expressed as Z/r^2 , where Z is a function of the cationic charge and r is the ionic radius [37,44]. In general, the greater the polarising power of the metal cation the stronger the attraction between it and non-bridging oxygens (NBOs), and hence the greater the tendency towards clustering of these metal cations and the occurrence of phase separation [44]. There are two mechanisms by which phase separation can occur in a glass melt: (i) spinodal decomposition; and (ii) nucleation and growth [38]. Spinodal decomposition typically results in a morphology that is three-dimensionally interconnected, consisting of two immiscible phases [39]. The nucleation and growth mechanism results in a morphology that consists of isolated spheres of the equilibrium composition randomly distributed throughout the matrix of another equilibrium composition [39], as demonstrated by Munoz et al. [33] who reported P_2O_5 -doped sodium borosilicate glasses that exhibited opalescence due to amorphous phase separation, displaying a droplet-like microstructure when analysed by SEM.

The presence of P_2O_5 has the effect of de-polymerising pure SiO_2 melts, yet it polymerises more compositionally-complex silicate melts in which additional metal cations, such as Na^+ , are present [13]. Chromatographic and spectral studies of phosphate and silicate glasses indicate that P^{5+} co-polymerises with the silicate network, decreasing silica activity due to the substitution of silica tetrahedra by phosphate tetrahedra [13]. When P_2O_5 is added to pure silica glass systems it has been shown to de-polymerise into mono- and diphosphates, resulting in the silicate network re-polymerising [25,36]. De-polymerisation also occurs when P_2O_5 is added to alkali borosilicate glass systems, wherein some phosphate units can also be bonded to borate units, forming P-O-B bonds [33]. The speciation of P^{5+} has been elucidated by magic angle spinning nuclear magnetic resonance spectroscopy (MAS-NMR) investigation with characteristic resonances at 15, 3 and -7.5 ppm, where 15 ppm and 3 ppm are attributed to mono- and diphosphates, respectively, with -7.5 ppm being attributed to P-O-B linkages [10,29]. Dupree et al. [40] found that in the case of sodium disilicate glasses with P_2O_5 additions, there were two distinct MAS-NMR resonances at ~ 15 and ~ 2.5 ppm. As the P_2O_5 content increased, the 2.5 ppm resonance increased in intensity while the 15 ppm decreased in intensity. Similar behaviour was observed for potassium disilicate glasses. The initially higher chemical shift values (ppm) in the different glasses were associated with alkali metal orthophosphates, while the lower chemical shift values were associated with pyrophosphates. The concentration of pyrophosphate units increases with higher P^{5+} concentrations, where there is a higher degree of polymerisation of the phosphate units. The degree of polymerisation depends on the changing abundance ratio between alkali cations and P^{5+} cations. Raman spectroscopic data for sodium silicate glasses has indicated the presence of phosphate units, i.e., Na_3PO_4 (orthophosphate) with higher concentrations (>5 mol%) of P_2O_5 leading to $\text{Na}_4\text{P}_2\text{O}_7$ (pyrophosphates) [40]. Stone-Weiss et al. [35] reported that for a $\text{Na}_2\text{O-P}_2\text{O}_5\text{-B}_2\text{O}_3\text{-SiO}_2$ glass system, where the ^{31}P MAS NMR spectra were fitted with six Gaussian components, they were attributed as follows: component one was attributed to $\text{P}_{1\text{B(V)}}^1$, component two was $\text{P}_{1\text{P}}^1$, component three was $\text{P}_{2\text{B}}^2$, components four and five were $\text{P}_{1\text{B}}^2$, 1P and $\text{P}_{2\text{B}}^2$, 1P , and component six was isolated monophosphate (P^0) or $\text{P}_{2\text{P}}^2$ chain phosphate species, with no linkages to boron. The superscript

refers to how many other structural units the phosphorus is bonded to and the subscript refers to the species to which they are bound. Lu et al. [41] investigated glasses with the composition $25\text{Na}_2\text{O}-25\text{Al}_2\text{O}_3-10\text{B}_2\text{O}_3-40\text{SiO}_2$ (mol%) doped with P_2O_5 concentrations of 0 to 15 mol%. The glass compositions were divided into three sub-classes with varying $\text{P}_2\text{O}_5/\text{Al}_2\text{O}_3$, $\text{P}_2\text{O}_5/\text{SiO}_2$, and $\text{P}_2\text{O}_5/\text{B}_2\text{O}_3$ ratios. In general, the ^{31}P MAS NMR spectra of all glasses exhibited peaks around -10 ppm and -2 ppm, which were attributed to PO_3^- and $\text{P}_2\text{O}_7^{4-}$ units, respectively. Metaluminous glasses with varying $\text{P}_2\text{O}_5/\text{B}_2\text{O}_3$ and $\text{P}_2\text{O}_5/\text{SiO}_2$ ratios exhibited spectra with peaks at -10 ppm and weak shoulders at -2 ppm. The increase in P_2O_5 content led to the formation of small fractions of P^3 and P^4 units. There was also little change in the line shape of the spectra, suggesting that the increase in P_2O_5 content had little effect on the phosphate environment, which may have been due to the unavailability of Na^+ cations in the glassy network.

Munoz et al. [34] established that the relationship between phase separation and the nature of phosphate species in sodium borosilicate glasses with high concentrations of SiO_2 and Na_2O , resulted in phase separation followed by crystallisation. Sodium borosilicate glasses with low Na_2O contents contained phosphate units that were mainly connected to the borate sub-network via P-O-B linkages and these glasses exhibited amorphous phase separation [34]. In such cases, the introduction of P_2O_5 can alter the phase separation mechanism from spinodal decomposition to nucleation and growth [14,34]. The occurrence of liquid-liquid (L-L) phase separation in silicate glasses is enhanced with the addition of P_2O_5 , with its occurrence predicted by the field strength of the network-forming ions, using the equation $F = Z/r^2$ [42,43]. The ionic field strength of P^{5+} and Si^{4+} have been calculated to be 43.2 and 23.8 a.u., respectively [43]. Consequently, the competition between the P^{5+} and Si^{4+} in attracting oxygens causes phase separation during the cooling period, leading to formation of phosphate-rich and silicate-rich phases [42].

Taylor [44] reviewed phase separation in borosilicate glasses relevant to nuclear fuel waste immobilisation, observing that phase separation of glasses normally occurs in a liquid that is either stable or supercooled, where a phase separated glass is the product of cooling a phase separated liquid [28]. The length scale of phase domains within the phase separated glass is dependent upon the thermal history of the glass and the relationship between viscosity and temperature, where high viscosity results in a slower rate of phase growth [44]. Stable macroscopic phase separation produces domains that are macroscopic and visible to an unaided eye, whilst sub-liquidus phase separation produces domains of $0.1\text{--}5\ \mu\text{m}$ [44]. Phase separation at this scale is detectable by visible opalescence and can be studied in further detail using SEM or transmission electron microscopy (TEM) [44]. Ultrafine phase separation is unavoidable, even when the glass melt has been rapidly quenched through the sub-liquidus miscibility gap to below T_g [44]. Hence, this length-scale of phase separation is best detected by small angle X-ray scattering (SAXS) [44]. One concern relating to phase separation in nuclear waste glasses is that it may reduce the chemical durability of the final vitrified wasteform, in which metal oxides and fission products can separate into the more soluble alkali + boron rich phase [44]. Therefore, phase separation should ideally be avoided at a level that causes negative dissolution behaviour by controlling the glass composition [44]. Hence, the P_2O_5 constraint in relevant HLW and LAW glass compositions has been outlined in different PNNL reports by Langowski [45], McCloy and Vienna [46], Vienna et al. [47], and Kruger et al. [6] with values of 3.0 wt% [45], ≤ 4.5 wt% [46,47], and ≤ 3.0 wt% [6], respectively. The P_2O_5 limit proposed by Langowski [45] was based on HLW quenched glasses that did not exhibit crystallinity or segregation. However, they also reported that <3.0 wt% P_2O_5 caused issues in PSCM-19 glasses, but in PSCM-9 glasses >4.0 wt% P_2O_5 was added with no melter issues [45]. The P_2O_5 constraints proposed by McCloy and Vienna [46] was based on a full HLW waste glass with 62 components, and those proposed by Vienna et al. [47] were based on HLW glass simulants with 15 main components, where the results contributed to

the modelling of glass properties [46,47]. The lower P_2O_5 value proposed by Kruger et al. [6] was a result of calculated property-composition models for ILAW-specific compositions with 64 components, where the maximum model validity range was between $0.0\text{--}3.0$ wt% P_2O_5 [6]. Hence, the limit for P_2O_5 in HLW glasses is between $\sim 3.0\text{--}4.5$ wt%, whilst in LAW glasses it is ≤ 3.0 wt%.

Makishima et al. [48] reported that for a quenched $10\ \text{Na}_2\text{O}-50\ \text{B}_2\text{O}_3-40\ \text{SiO}_2$ (wt%) glass system doped with 5 wt% P_2O_5 , the resulting sample was opacified [49]. Similarly, Schuller et al. [11] investigated phase separation and crystallisation of borosilicate glasses enriched in MoO_3 , P_2O_5 , ZrO_2 and CaO , where glasses that contained 3.7 wt% P_2O_5 and were either plate-quenched, roller-quenched or air-blown, produced a morphology of spherical separated phases, characteristic of phase separation via the nucleation and growth mechanism [11]. Langowski [45] described work by Vogel [50,51] stating that the addition of P_2O_5 into $\text{Na}_2\text{O}-\text{B}_2\text{O}_3-\text{SiO}_2$ glasses resulted in a droplet phase rich in P_2O_5 , where the phase separation could either be liquid-liquid or liquid-crystal. It was noted that additions of CaO to this glass system with 2.5 wt% P_2O_5 increased the phase separated droplet size, where CaO was found concentrated in said droplets, causing secondary precipitation of an apatite phase [45,50,51]. Munoz et al. [34] reported the effects of P_2O_5 on a $\text{Na}_2\text{O}-\text{B}_2\text{O}_3-\text{SiO}_2$ glass system, where the glasses were first quenched before being thermally treated at $650\ ^\circ\text{C}$ for 48 h to induce phase separation: these glasses incorporated 3.0 mol% P_2O_5 [34]. O'Donnell et al. [52] reported on the effects of phosphorus in two series of bioglasses in the quaternary system $\text{SiO}_2-\text{Na}_2\text{O}-\text{CaO}-\text{P}_2\text{O}_5$. These glasses were annealed overnight and some displayed phase separation and / or crystallisation. Dilatometric measurements that could be conducted on non-phase separated / crystallised samples revealed T_g 's of $482\ ^\circ\text{C}$ to $515\ ^\circ\text{C}$ [52]. Fábán et al. [53] investigated bioactive glasses in the $\text{SiO}_2-\text{CaO}-\text{Na}_2\text{O}-\text{P}_2\text{O}_5$ system with P_2O_5 contents of 0 to 5 mol%. The samples were melt-quenched, with T_g of $516\text{--}550\ ^\circ\text{C}$, and T_x of $662\text{--}754\ ^\circ\text{C}$. The glasses became phase separated above 3 mol% P_2O_5 which was indicated by the fall in T_x for the 5.0 mol% sample [53]. Soleimanzade et al. [54] investigated phase separation in $\text{SiO}_2-\text{B}_2\text{O}_3--\text{Na}_2\text{O}-\text{ZnO}-\text{Al}_2\text{O}_3-\text{P}_2\text{O}_5$ glasses where opacification occurred at 2 wt% P_2O_5 when the glass was heat treated at $800\ ^\circ\text{C}$, whilst the 4 wt% P_2O_5 sample opacified spontaneously during melt casting. The increase in P_2O_5 content saw a transformation of the immiscibility mechanisms from nucleation and growth to spinodal decomposition [54]. Literature has thus demonstrated that not only glass composition affects the P_2O_5 solubility and subsequent phase separation, but also heat treatment or the lack thereof can also affect it, where annealing samples can induce or accelerate phase separation and crystallisation due to samples being held at $T > T_g$ of one of the phases present, enabling formation of nuclei and their subsequent growth [55].

The other effects of P_2O_5 on oxide glass systems include thermal and chemical properties. Examinations of silicate melts and glass structure at high temperatures show that increasing temperatures above T_g lead to a gradual change in the proportion of silicate structural units [56]. Mysen [57] investigated Na-silicate melts containing 2.0 mol% P_2O_5 and found that speciation was highly dependent on temperature, with P_2O_5 species converting from orthophosphate to pyrophosphate as the temperature increased through the T_g range [57]. Rheological properties of glass melts are dependent on the structural arrangements within the melt [58]. In a peralkaline melt with metal cations, the additions of phosphorus leads to the removal of these metal cations from the silicate network, resulting in its polymerization, which affects viscosity, causing it to increase [29]. The increased polymerization means that there is a decrease in abundance of NBOs because of the formation of phosphorus-oxygen anionic species and their incorporation into the silicate network [59]. The changes in viscosity caused by additions of P_2O_5 may provide indications of change in the average bond strength in the melt, implying that: (i) the 'different solution mechanisms of phosphorus should have different effects on the melt viscosity' [29]; and (ii) the extent of these effects may be related to the enthalpic consequences

of adding P₂O₅ [29]. Additions of 1 wt% P₂O₅ to a soda-lime-silica glass system led to a slight increase in the dilatometric softening temperature (T_d), but not in viscosity, coefficient thermal expansion (CTE) and T_g [60].

2. Materials and methods

Note regarding nomenclature: In Section 1 concentrations were described in either mol% or wt%. In these results and subsequent discussion, the concentrations will use the nomenclature 'NBSP' where the following number represents the nominal P₂O₅ content in mol% e.g., NBSP1.0 = 1.0 mol%. The 'NBSP' initials are derived from the cations in the formula Na₂O-B₂O₃-SiO₂-xP₂O₅ of the glass compositions.

This glass series is a simplification of HLW and LAW Hanford radioactive waste glasses [1,5,6] as the original compositions were too complex, with many components, to allow meaningful structural analysis, for example by Raman spectroscopy. To understand the effects of P₂O₅ on an alkaline borosilicate glass a simple glass system was needed, hence sodium borosilicate was selected.

100 gramme batches of the NBSP glasses were prepared by using the melting-annealing and melting-quenching methods using analytical-grade precursors of SiO₂, Na₂CO₃, H₃BO₃ and NH₄H₂PO₄. The precursors were weighed and transferred to a plastic tub that was thoroughly shaken to mix the contents, before being milled in an agate mill for one minute to achieve a fine, homogenous mixture. The mixture was then placed in a (90%:10%) platinum (Pt)-Rhodium (Rh) crucible and heated in an electric furnace at 1150 °C for one hour, after which part of the melt was removed and air-quenched on a steel plate, then left to cool to room temperature. The remainder of the melt was cast into a steel mould that was pre-heated on a hot plate, before it was transferred to an annealing furnace at 500 °C to dwell for one hour, then cooled with a controlled cooling rate of 1 °C min⁻¹ to 25 °C. For electron microscopy, the annealed samples were cut using a diamond saw, and then either mounted on a scanning electron microscope (SEM) stub or suspended in a conductive graphite epoxy. The samples were then ground using sandpaper (grit size: 60 mm, 240 mm, 320 mm, 600 mm, 800 mm and 1200 mm) and polished with polycrystalline diamond slurry suspension (15 µm, 9 µm, 3 µm and 1 µm).

X-ray fluorescence (XRF) samples were prepared by mixing approximately one gramme of the sample powder with ten grammes of lithium tetraborate fusion flux (doped with 0.5% LiI anti-cracking agent) in a platinum crucible, before being placed in the LeNeo automatic fusion system at 1065 °C for 20 min, then being poured and cooled. The samples were then analysed using a Bruker XRF S4-Pioneer X-ray Fluorescence spectrometer which employed a modified OXI method [61], with the results provided being estimates based on calculated values because this XRF cannot report lighter elements such as lithium and boron, hence the values were pro-rated with nominal values of B₂O₃. However, inductively coupled plasma optical emission spectroscopy (ICP-OES) was conducted externally in accordance with the UKAS accredited ICP-OES-ATM 83 standard to measure the boron content of three samples (NBSP 0.0, 3.0, and 4.0) to confirm that nominal and analyzed boron contents were similar.

X-ray (powder) diffraction (XRD) patterns of powdered annealed and quenched samples were recorded using CuKα radiation on a Bruker D8 Advance diffractometer with step size of 0.015°2θ; scan step time of 177 s; and were measured between 5° and 70°2θ and plotted between 10 and 70°2θ. The X-ray diffraction patterns of the Canister Centerline Cooling (CCC) heat-treated samples were recorded using CuKα radiation on a PANalytical X'Pert Pro-MPD with step size of 0.013°2θ; scan step time of 199 s; and were measured between 5° and 80°2θ and plotted between 10 and 80°2θ.

The SEM samples were prepared by suspending a shard of glass in graphite epoxy resin, after which the samples were ground using grit sizes 240–2400 and polished using 6 µm and 1 µm diamond suspension to a mirror finish. The samples were then mounted onto an SEM stub

using silver paint, after which the samples were carbon coated, because glasses are non-conductive. Electron micrographs were acquired using a FEI Nova Nanosem 200 Field Emission Gun Scanning Electron Microscope (FEG-SEM). The images were collected in backscattered electron (BSE) mode utilizing a solid-state backscattered electron detector. An electron beam energy of 15 keV and spot size between 4 and 5, were used in order to maximise resolution and image quality, whilst minimizing electron beam damage to the specimens. All images were acquired at 60,000 times magnification.

For T_g measurements, dilatometry and DTA were used to heat the sample to 800 °C and 625 °C, respectively, at a rate of 10 °C min⁻¹. Dilatometry also determined three other features: (i) T_g onset, (ii) dilatometric softening point, T_d, and (iii) the linear coefficient of thermal expansion (CTE), α. An SDT Q600 V20.9 build 20 and NETZSCH DIL 402SE dilatometer were used. High-temperature viscosity (HTV) was measured using an Anton Paar FRS (Furnace Rheometer system) 1600. Raman spectroscopy was conducted using a Renishaw CCD Camera Raman spectrometer with a laser wavelength of 514.5 nm. The samples had an exposure of 10 s at 3 accumulations with a laser power of 100% using a 2400 L/mm grating and a magnification of 50x. The spectra were corrected using the onboard sonic ray removal application. The samples had measurements taken at three different locations so that an average could be calculated. The spectra were then corrected for temperature and excitation line effects using the Neuville and Mysen method [62] (1):

$$I = I_{obs} \cdot [V_0^3 [1 - \exp(-hcv/kT)]v / (v_0 - v)^4] \quad (1)$$

Where h is the Planck constant, k is the Boltzmann constant, c is the speed of light, T is the absolute temperature, v_0 is the wavenumber of incident laser light, and v is the measured Raman shift.

3. Results

3.1. Visual observations

The sample glasses (Fig. 1) obtained after annealing resulted in bubbly, transparent, relatively homogeneous glasses with an amorphous structure, as confirmed by XRD (Fig. 4). However, increasing P₂O₅ contents led to a decrease in the glass-forming abilities of the material, resulting in visually opaque samples (Figs. 1 and 2). Fig. 2 does illustrate that the sample is not homogeneous due to the presence of opalescence in only part of the sample and not its entirety, and may indicate heterogeneity in the glass composition and / or a temperature gradient during cooling / annealing. Phase separation occurred visually at a macroscopic scale as opalescence in samples containing >4.0 mol% P₂O₅, which gives a bluish and creamy-white colour (Figs. 1 and 2). The occurrence of opalescence is due to the presence of one or more secondary phases with a different refractive index to the bulk glass matrix, and as a result they act as scattering centres [58]. Opalescence often occurs as a bluish colour because the Rayleigh scattering associated with the size of the crystalline particles is smaller than or similar to the minimum wavelength of visible light [58]. Table 1 and Fig. 3 present the nominal and analysed compositions of the annealed and quenched NBSP samples, as measured by XRF and ICP-OES.

3.2. X-ray fluorescence (XRF)

Table 1 contains the nominal and XRF and ICP-OES analysed compositions of the annealed and quenched glass samples. While both sets of glasses originated from the same melts, it can be seen that there are small deviations in the analyzed contents of SiO₂, Na₂O, and P₂O₅, indicating that the melts may have exhibited a degree of inhomogeneity although experimental uncertainties associated with the analyses can also be expected to play a role. Analysis of the quenched samples were performed to better inform understanding of the effects of thermal

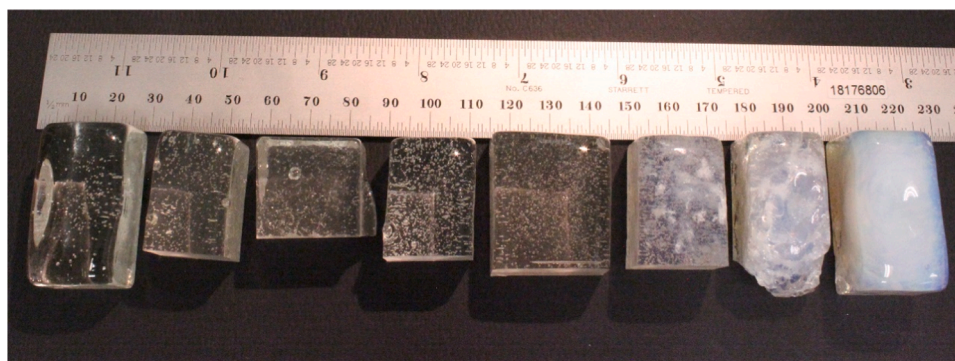


Fig. 1. Annealed NBSP glass samples (0.0 (left) to 6.0 (right) nominal mol (%) P_2O_5) with a ruler to act as a scale marker and visual guide of the level of opalescence in the samples.

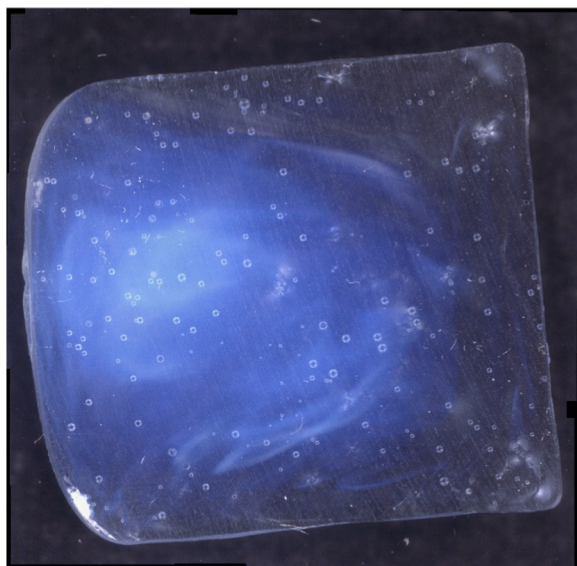


Fig. 2. Cross-section optical image of sample NBSP6.0 at 50x magnification to illustrate opalescence.

treatment and any resulting crystallisation behaviour.

Fig. 3 plots the XRF and ICP-OES analysis results for the annealed samples, where the associated uncertainties are recorded in Table 1. ICP-OES was only used to measure the boron content of the annealed samples NBSP 0.0, 3.0 and 4.0, due to equipment and time restraints, as they were the samples for which the solubility limit was determined to lie between. The analysed SiO_2 , Na_2O , and P_2O_5 contents varied between

50.7 and 57.4 mol%, 25.2 and 28.0 mol%, and 0.0 and 6.5 mol%, respectively. When compared to the nominal compositions, the SiO_2 content of samples NBSP 0.0 and 5.0 were comparable within error, whereas for samples NBSP 1.0 and 2.0 they were slightly higher, and for samples NBSP 3.0, 4.0, 5.5, and 6.0 they were slightly lower. The Na_2O content of samples NBSP 0.0, 1.0, 2.0, 3.0, 4.0, 5.0, and 6.0 were comparable to the nominal compositions within experimental uncertainties, whereas for sample NBSP 5.5 it was higher by 3.44 mol%. The P_2O_5 contents of samples NBSP 1.0, 2.0, 3.0, 4.0, 5.0, and 5.5 were all comparable with their nominal compositions within experimental uncertainties, but for the NBSP 6.0 sample it was slightly elevated by 0.5 mol%. The differences in measured concentrations of the XRF-analysed components may be a result of the heat treatment of the glass, for which part of the glass melt was poured and analysed, i.e., from the top, middle or bottom of the crucible, or any uncertainties associated with preparation and analysis by XRF. Other sources of uncertainty may be due to volatilisation of P_2O_5 and Na_2O during melting, the section of the sample used for the XRF fused bead, where samples with >3.0 mol% P_2O_5 presented evidence of phase separation and crystallisation, meaning the sample may not have been completely homogeneous. Another potential cause for minor fluctuations in the composition may be contamination during sample preparation.

The ICP-OES analysed B_2O_3 contents of the NBSP 0.0, 3.0, and 4.0 samples were $16.3 \pm 1\%$, $19.2 \pm 1\%$, and $15.9 \pm 1\%$ mol%, respectively. Sample NBSP 0.0 content was comparable to the nominal content within experimental uncertainties, whereas for the NBSP 3.0 sample it was significantly higher by 3.41 mol% and for the NBSP 4.0 it was marginally higher than the nominal content by 0.27 mol%. The variations in B_2O_3 content of the samples measured by ICP-OES may be due to the sample not being completely homogeneous, where the sample used had a variation in composition to another section. Another source of

Table 1
Nominal vs. analysed glass compositions.

Oxides		Sample							
		NBSP0.0	NBSP1.0	NBSP2.0	NBSP3.0	NBSP4.0	NBSP5.0	NBSP5.5	NBSP6.0
Na_2O	Nominal (mol%)	27.91	27.63	27.35	27.07	26.79	26.51	24.56	26.23
	Analysed Annealed (mol%)	28.2 ± 1.1	25.2 ± 2.2	26.7 ± 1.6	26.4 ± 1.3	27.53 ± 1.2	25.9 ± 1.2	28.0 ± 1.2	27.4 ± 1.7
	Analysed Quenched (mol%)	28.4 ± 1.1	28.3 ± 1.2	27.7 ± 1.2	27.5 ± 1.2	27.2 ± 1.2	27.9 ± 1.2	28.1 ± 1.2	27.1 ± 1.2
B_2O_3	Nominal (mol%)	16.28	16.12	15.95	15.79	15.63	15.47	15.38	15.30
	Analysed Annealed by ICP-OES (mol%) $\pm 1\%$	$16.3 \pm 1\%$	–	–	$19.2 \pm 1\%$	$15.9 \pm 1\%$	–	–	–
SiO_2	Nominal (mol%)	55.81	55.26	54.70	54.14	53.58	53.02	52.74	52.47
	Analysed Annealed (mol%)	55.5 ± 0.5	57.7 ± 0.9	55.2 ± 0.7	51.6 ± 0.6	52.5 ± 0.5	53.9 ± 0.5	50.9 ± 0.5	50.7 ± 0.8
	Analysed Quenched (mol%)	55.4 ± 0.5	54.6 ± 0.5	54.3 ± 0.5	53.7 ± 0.5	53.0 ± 0.5	51.5 ± 0.5	51.0 ± 0.5	52.0 ± 0.5
P_2O_5	Nominal (mol%)	0.00	1.00	2.00	3.00	4.00	5.00	5.50	6.00
	Analysed Annealed (mol%)	0.0	1.0 ± 4.3	2.1 ± 2.2	2.7 ± 1.5	4.0 ± 1.2	4.9 ± 1.2	5.7 ± 1.2	6.5 ± 1.7
	Analysed Quenched (mol%)	0.0	1.1 ± 2.2	2.1 ± 1.6	3.0 ± 1.3	4.2 ± 1.1	5.2 ± 1.0	5.6 ± 1.0	6.2 ± 0.9

* B_2O_3 nominal values used, due to boron being undetected by the XRF spectrometer used, except for samples NBSP0.0, 3.0, and 4.0 for which ICP-OES analyses were obtained.

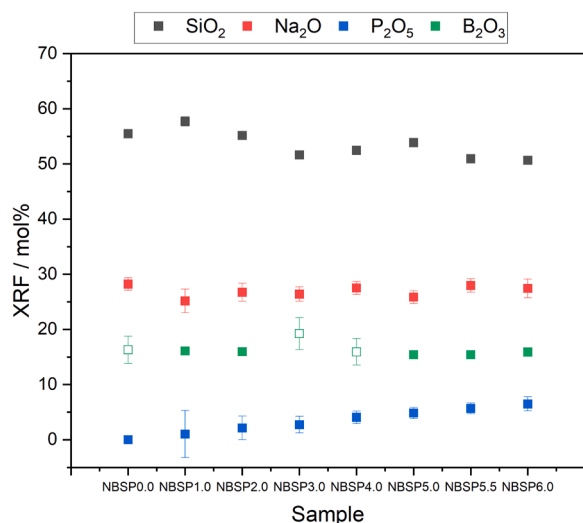


Fig. 3. Graphical representation of XRF results for annealed NBSP samples, where hollow markers represent B_2O_3 analysed by ICP-OES, with associated errors shown in Table 1. Where error bars are not present, this is because they are smaller than the data markers.

uncertainty may be related to the ICP-OES technique, where signal drift, spectral interferences, or the inaccurate signal identification may affect the results.

3.3. X-ray diffraction (XRD)

3.3.1. Annealed samples

Fig. 4 shows that samples NBSP 0.0, 1.0, 2.0 and 3.0 were X-ray amorphous with no measurable crystallinity, whilst samples NBSP 4.0, 5.0, 5.5 and 6.0 produced measurable Bragg reflections, evidencing identifiable crystalline phases present within the amorphous material. Sample NBSP 4.0 exhibited the crystalline phase sodium phosphate (Na_3PO_4 , PDF#: 01-071-1918); sample NBSP 5.0 exhibited sodium phosphate (Na_3PO_4 , PDF#: 01-071-1918) and ($Na_4P_2O_7$, PDF#: 01-073-5982); sample NBSP 5.5 exhibited sodium phosphate (Na_3PO_4 , PDF#: 01-071-1918), ($Na_4P_2O_7$, PDF#: 01-073-5982) and cristobalite (SiO_2 , PDF#: 01-074-9378); and sample NBSP 6.0 exhibited sodium phosphate (Na_3PO_4 , PDF#: 01-071-1918) and ($Na_4P_2O_7$, PDF#: 01-073-5982). The crystal structure of the Na_3PO_4 was face centred cubic (fcc), where the phosphorus sites are fully occupied while the sodium and oxygen sites are only partially filled. The $Na_4P_2O_7$ possesses

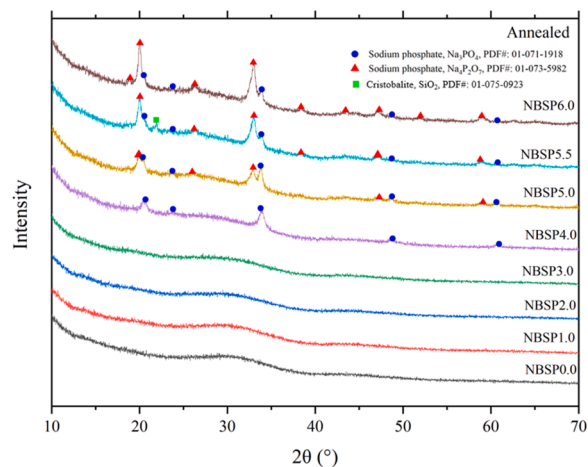


Fig. 4. XRD patterns for annealed NBSP glass samples with identified crystalline phases listed.

an orthorhombic crystal structure where all its sites are fully occupied. The identification of a strong Bragg peak at $\sim 22^\circ 2\theta$ in the XRD pattern for sample NBSP 5.5 was tentatively attributed to SiO_2 (visually verified) (cristobalite, PDF#: 01-074-9378).

3.3.2. Air quenched samples

Fig. 5 shows the XRD patterns for the quenched samples, with samples NBSP 1.0, 2.0 and 3.0 being confirmed to be X-ray amorphous with no measurable crystallinity. Samples NBSP 4.0, 5.0, 5.5, and 6.0 exhibited measurable Bragg peaks and identifiable crystalline phases present within the amorphous material. Sample NBSP 4.0 showed evidence of a small Bragg reflection at $\sim 22^\circ 2\theta$. Although this was not positively identified, it is consistent with the peaks attributed to cristobalite (SiO_2 ; PDF#: 01-071-3839) for the higher- P_2O_5 samples. Samples NBSP 5.0, NBSP 5.5 and NBSP 6.0 contained the phases sodium phosphate ($Na_4P_2O_7$; PDF#: 01-073-5982) and cristobalite (SiO_2 ; PDF#: 01-071-3839). There was also a shoulder peak beside the characteristic $Na_4P_2O_7$ Bragg peak ($\sim 20^\circ 2\theta$) at $\sim 20.5^\circ 2\theta$ which, when compared with the annealed samples, was consistent with an identified Na_3PO_4 Bragg peak. Hence, these peaks have been labelled as Na_3PO_4 . As the P_2O_5 content increased, the simultaneous presence of Na_3PO_4 and $Na_4P_2O_7$ characteristic Bragg peaks in the XRD patterns for the NBSP 5.0–6.0 samples indicated an increase in the relative intensity of $Na_4P_2O_7$ peaks.

3.3.3. Canister centreline cooling (CCC) samples

Further to the observation that annealing can impact on phase separation/crystallization behaviour (Sections 4.1.1. and 4.1.2), and in order to better understand the behaviour of the studied glasses under an imposed heat treatment regime relevant to nuclear waste vitrification, we have undertaken Canister Centerline Cooling (CCC) experiments. In the steel canisters into which Hanford HLW glasses will be poured, the melt is expected to cool slowly from the melter operating temperature of $1150^\circ C$ to ambient temperatures [63,108]. The centreline of the canister is where it is expected that crystallisation will occur and be at its greatest, where cooling is slowest [106]. In the case of HLW glasses, it has been shown that the cooling regime promotes crystallisation of aluminosilicate phases such as nepheline and spinel [65,67,69,63]. The presence of nepheline is problematic in HLW glass because it can decrease the chemical durability of the final immobilized vitrified form by removing Si and Al from the glass network [65,67,69,63], whilst spinel crystallisation during melting may cause shorting of electrodes and block the melter discharge port [66,68]. In order to replicate the behaviour of the slowest cooled area in the canister, the CCC thermal profiles (Tables 2 and 3) were developed by Savannah River National

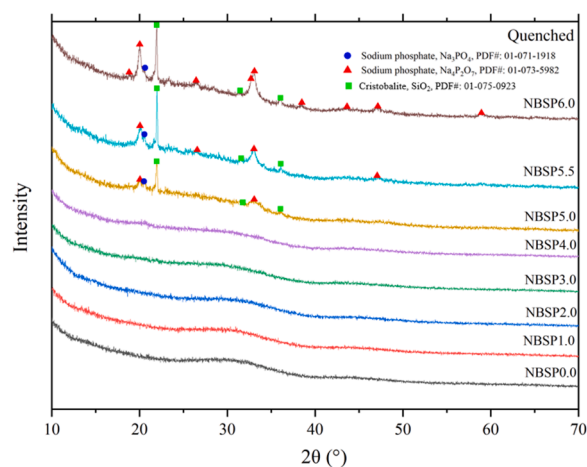


Fig. 5. XRD patterns for quenched, unannealed NBSP glass samples with identified crystalline phases listed.

Laboratory (SRNL) [70,71] to model the worst-case scenario for the occurrence of crystallisation. Both HLW [71] and LAW [70] CCC heat treatment regimes were performed on all NBSP samples.

Fig. 6 shows the XRD patterns for the HLW CCC NBSP glasses. Samples NBSP 0.0, 1.0 and 2.0 were X-ray amorphous, whilst sample NBSP 3.0 showed evidence of some degree of crystallinity present within the amorphous material (Fig. 6). As the P_2O_5 content increased, the samples gradually became more crystalline. Sample NBSP 3.0 exhibited sodium phosphate (Na_3PO_4 , PDF#: 01-071-1918) but also presented a peak at $\sim 26^\circ 2\theta$, which corresponds to the strongest intensity peak of quartz (SiO_2 , PDF#: 01-089-1961), where its presence in this sample may be due to unmelted silica. Sample NBSP 4.0 exhibited sodium phosphate (Na_3PO_4 , PDF#: 00-031-1318), sample NBSP 5.0 exhibited sodium phosphate (Na_3PO_4 , PDF#: 00-03-1318 and $Na_4P_2O_7$, PDF#: 04-018-4331) with evidence of the characteristic cristobalite peak at $\sim 23^\circ 2\theta$ albeit weak in intensity; sample NBSP 5.5 exhibited sodium phosphate (Na_3PO_4 , PDF#: 00-031-1318 and $Na_4P_2O_7$, PDF#: 04-018-4331) and cristobalite (SiO_2 , PDF#: 00-039-142); and sample NBSP 6.0 exhibited sodium phosphate (Na_3PO_4 , PDF#: 00-031-1318 and $Na_4P_2O_7$, PDF#: 00-010-018) and cristobalite (SiO_2 , PDF#: 00-039-142). The Na_3PO_4 exhibited a cubic structure, whilst $Na_4P_2O_7$ was either orthorhombic or hexagonal and SiO_2 was tetragonal.

Fig. 7 shows the XRD patterns for the LAW CCC NBSP glasses. Samples NBSP 0.0 to NBSP 3.0 are shown to be X-ray amorphous. As with the HLW CCC NBSP glasses, as P_2O_5 content increased the degree of crystallinity of the samples increased. However, the “onset” of crystallinity occurred at higher P_2O_5 contents in the LAW CCC treated samples than the HLW CCC treated samples. Sample NBSP 4.0 exhibited Na_3PO_4 (PDF#: 00-031-1318) and a weak intensity peak characteristic of cristobalite; sample NBSP 5.0 exhibited Na_3PO_4 (PDF#: 00-027-0771) and $Na_4P_2O_7$ (PDF#: 00-010-0187); and samples NBSP 5.5 and 6.0 exhibited $Na_4P_2O_7$ (PDF#: 04-018-4331) and SiO_2 (cristobalite and tridymite) (PDF#: 04-008-4812 and 04-012-1333). There was also evidence of similar characteristic Bragg peaks for Na_3PO_4 as in the previous samples, but this phase was not officially identified using HighScore Plus because of the weak peak intensity and overlap with other peaks. Na_3PO_4 present in samples NBSP 4.0, 5.0, and 5.5 had the same cubic crystal structure. $Na_4P_2O_7$ in sample NBSP 5.0 had a hexagonal crystal structure, while in samples NBSP 5.5 and 6.0 it had an orthorhombic structure. The SiO_2 in the NBSP 6.0 sample was present as cristobalite and tridymite which had tetragonal and monoclinic crystal structures, respectively.

3.4. Scanning electron microscopy (SEM)

Figs. 8-12 show the backscattered SEM images of samples NBSP 3.0, 4.0 5.0, 5.5, and 6.0 at a magnification of 60000x. Samples NBSP 0.0–2.0 were X-ray amorphous and so were not SEM-analysed. SEM of sample NBSP 3.0 displayed a fully amorphous matrix with no evidence of droplets or other characteristics associated with phase separation or

Table 2

HLW canister centreline cooling schedule used, from [71].

Segment	Start Temperature (°C)	Stop temperature (°C)	Rate (°C/min)	Dwell (min)
1	1150	1150	0	30
2	1150	1050	Furnace quench	–
3	1050	980	1.6	–
4	980	930	0.8	–
5	930	875	0.6	–
6	875	825	0.4	–
7	825	775	0.3	–
8	775	725	0.3	–
9	725	400	0.3	–
10	400	0	Furnace quench	–

Table 3

LAW canister centreline cooling schedule used, from [70].

Segment	Start Temperature (°C)	Stop temperature (°C)	Rate (°C/min)	Dwell (min)
1	1150	1150	0	30
2	1150	1114	Furnace quench	–
3	1114	1000	7.1	–
4	1000	900	1.8	–
5	900	825	0.6	–
6	825	775	0.3	–
7	775	725	0.2	–
8	725	600	0.1	–
9	600	0	0.1	–

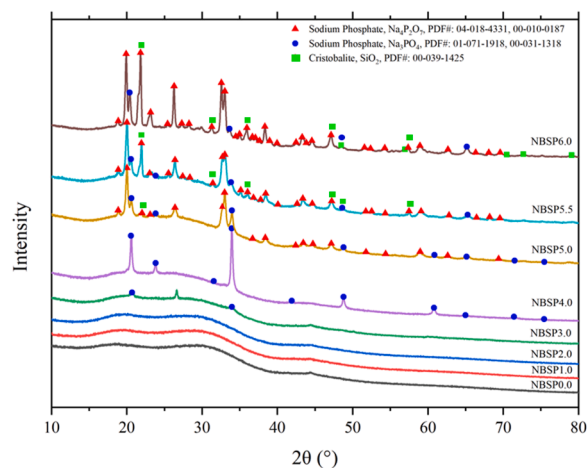


Fig. 6. XRD patterns for all samples and identified crystalline phases in NBSP 0.0 to 6.0 for HLW CCC heat treatment regime.

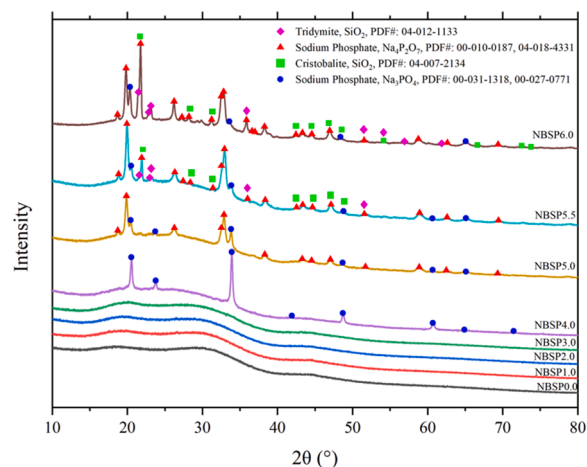


Fig. 7. XRD patterns for all samples and identified crystalline phases in NBSP 0.0 to 6.0 for LAW CCC heat treatment regime.

crystallisation. Samples NBSP 4.0–6.0 exhibited darker droplets in a lighter matrix, with small lighter crystal clusters growing from the droplets, however, without the use of energy-dispersive X-ray analysis (EDS) it cannot be confirmed which phases were present. EDS was not used because of the likelihood of beam damage to the samples at these high magnifications. However, the formation of these $<1 \mu m$, relatively uniformly separated droplets suggests that the glass composition is located in between the spinodal and binodal lines, where phase separation occurs as a nucleation-type mechanism [126]. The increase in size

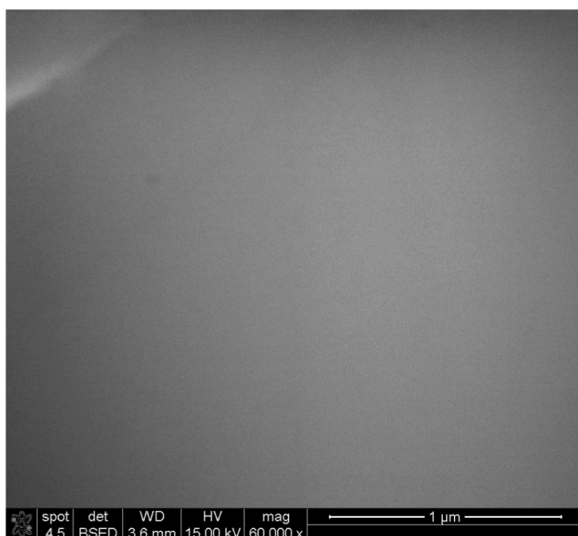


Fig. 8. Backscattered electron image of sample NBSP 3.0 at a magnification of 60,000x.

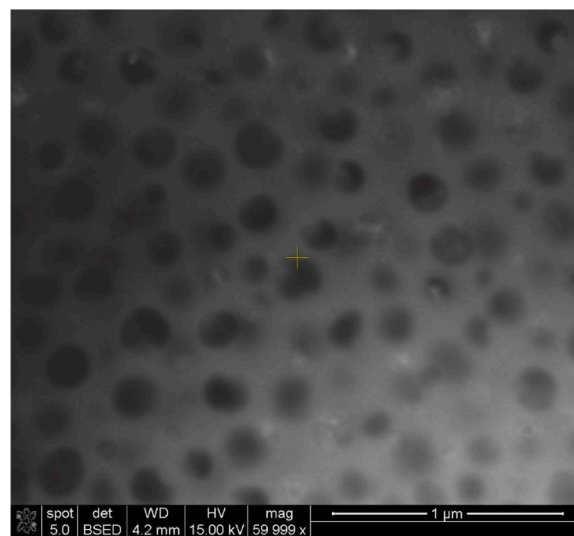


Fig. 10. Backscattered electron image of sample NBSP 5.0 at a magnification of 60,000x.

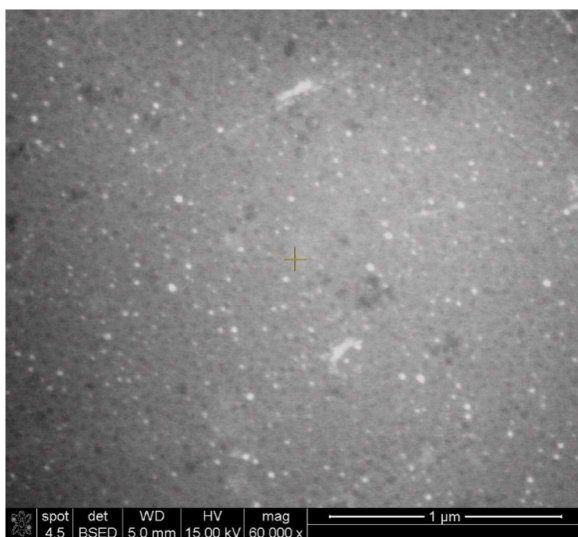


Fig. 9. Backscattered electron image of sample NBSP 4.0 at a magnification of 60,000x.

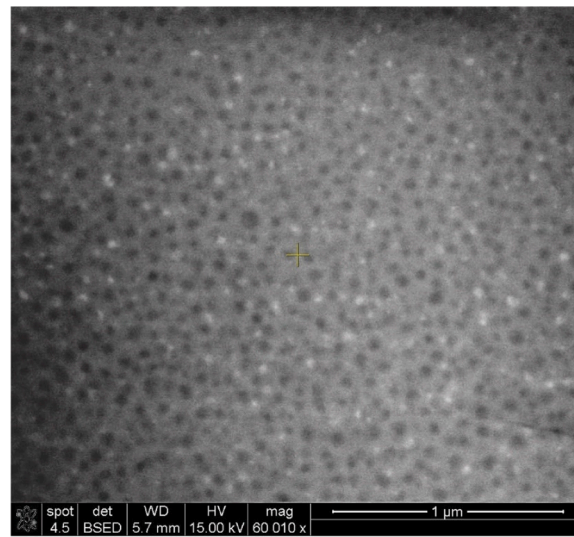


Fig. 11. Backscattered electron image of sample NBSP 5.5 at a magnification of 60,000x.

of some of the droplets with 4.0–6.0 mol% P_2O_5 additions may have been produced by the Ostwald ripening mechanism due to a diffusion process [16]. The display of two different shaded droplet types in the residual matrix (Figs. 8–12) suggests that they have different compositions. The original base glass was determined to not be susceptible to immiscibility given its position in the $Na_2O-B_2O_3-SiO_2$ ternary phase diagram, and the additions of P_2O_5 have enhanced the glasses' susceptibility to phase separation and crystallization [16].

3.5. Thermal parameters

DTA and dilatometry were conducted on the annealed samples, where the following figures exhibit graphical representations of this data. Fig. 8 shows the effects of increasing the P_2O_5 content on T_g (the onset T_g) based on values from Table 4. From analysing Fig. 13, the DTA T_g onset exhibits little change, within uncertainties, between 0.0 and 2.7 mol% P_2O_5 , but not between 2.7 and 6.5 mol% P_2O_5 . Instead, there is decrease at 4.0 mol% P_2O_5 followed by a sharp increase at 4.9 mol% P_2O_5 through to 6.5 mol% P_2O_5 . The dilatometry T_g onset shows a

similar trend to DTA, where between 0.0 and 2.7 mol% P_2O_5 , the T_g onset is the same, within uncertainties. However, this was followed by a sharp increase at 4.0 mol% P_2O_5 onwards, which is the same within uncertainties between 4.0 and 6.5 mol% P_2O_5 . The increase at 4.0 mol% P_2O_5 is consistent with the occurrence of the sodium phosphate crystal phases that were confirmed by XRD. Both sets of data follow similar trends, with an increase in the T_g onset with increasing P_2O_5 content.

Fig. 14 shows the effects of increasing the P_2O_5 content on the DTA T_g onset, T_d , CTE and viscosity at 950 °C based on values from Table 5. T_d is constant between 0.0 and 2.7 mol% P_2O_5 , within uncertainties, the same as the T_g onset. However, there is a sharp increase of 20 ± 5 °C between 2.7 and 4.0 mol% P_2O_5 , after which the increase between 4.0 and 6.5 mol% P_2O_5 is the same, within uncertainties. The CTE shows a decrease between 0.0 and 1.0 mol% P_2O_5 . There is then an increase between 2.1 and 2.7 mol% P_2O_5 and between 2.7 and 4.0 mol% P_2O_5 . The samples with 4.0 to 6.5 mol% P_2O_5 exhibit no further change in CTE, within uncertainties. The viscosity, exhibited via T_d , shows a general positive linear relationship with P_2O_5 content.

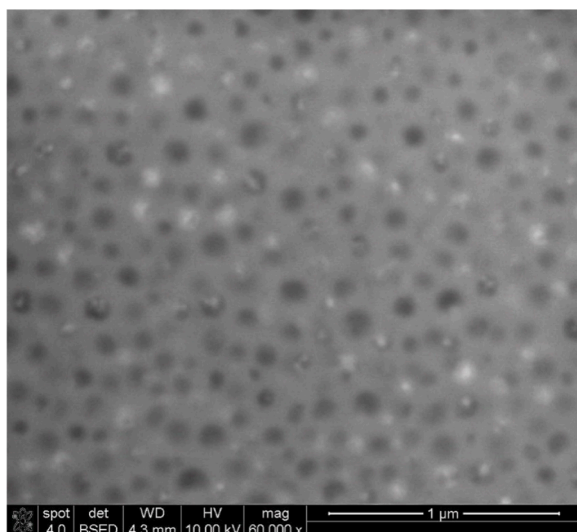


Fig. 12. Backscattered electron image of sample NBSP 6.0 at a magnification of 60,000x.

3.6. High temperature viscosity (HTV)

Fig. 15 depicts a line plot illustrating the measured viscosity at several temperatures for each NBSP glass melt, highlighting the effect of increasing P_2O_5 content. The general trend is a linear positive correlation, in that for a given temperature, as the P_2O_5 content increases, the viscosity of the melt increases. The increase in viscosity as the P_2O_5 content increases is indicative that the silicate network is re-polymerising, which is also consistent with the increases in both T_g and T_d (Fig. 14). The plot of the logarithm of viscosity versus the reciprocal of absolute temperature ($1/T$) produced a linear function (Fig. 15), and data could be reliably fitted with the Arrhenius-type equation ($\ln(\eta) = \ln(A_s) + (E_a/R) \cdot (1/T)$), where (E_a/R) is the gradient of the straight line, and $(\ln(A_s))$ is equal to the intercept of the y-axis [73]. The methodology reported by Messaadi et al. [73] was adopted, using both linear least-squares fitting and graphical methods in the Excel software package to establish the Arrhenius activation energy (E_a/R) and entropic factor of Arrhenius ($\ln(A_s)$) as a function of P_2O_5 content: the values are presented in Table 6. The Arrhenius activation energy (E_a) ranged between 16.429–22.826 KJ.mol^{-1} , whilst the entropic factor of Arrhenius ($\ln(A_s)$) ranged between -10.94 and -14.74 . The Arrhenius behaviour of the melts suggests that the increase in the P_2O_5 contents increased the activation energy for viscous flow due to the re-polymerization of the melt structure [74]. The Vogel-Fulcher-Tammann (VFT) equation was not implemented on the

viscosity data because it is used to fit data ranging between 10^3 and 10^{13} Pa.s and fails when viscosity values are $< 10^2$ Pa.s [72]; the viscosity data in this investigation ranged between -0.08495 and 1.72102 Pa.s (Table 5).

Figures S1-S4 in the supplementary material illustrate the rheological behaviour of the glass melts, with viscosity of a Newtonian fluid being independent of the shear rate, displaying a linear relation between shear rate and shear stress [76], whilst a non-Newtonian fluid displays a non-linear function of the shear rate [77]. Figures S1-S4 present the viscosity behaviour of the glass melts at 950 °C, 1050 °C, 1150 °C, and 1250 °C with increasing nominal P_2O_5 content, respectively. At 0.0 mol % P_2O_5 , the glass melt behaves as a fully Newtonian liquid at 950 and 1250 °C. However, there is a slight discrepancy in the data at 1050 and 1150 °C, when the shear rate was between 6.1 – 7.8 s^{-1} and 12.2 – 12.9 s^{-1} , respectively. The function was no longer linear, but instead exhibited a slight hysteresis loop, with this behaviour indicating that the glass melt was exhibiting shear thickening. Shear thickening is when the viscosity of the liquid increases with an increase in shear stress at a constant shear rate [76,78]. Such an effect can result in a jump in the shear stress on exceeding the “critical” shear rate, where the flow of the liquid becomes erratic, suggesting the formation and separation of stress supporting structures [75,76,79]. At 1.0 mol% P_2O_5 at 950 °C (Figure S1) the data shows little variance in the shear stress when compared to 0.0 mol% P_2O_5 , however, the shear stress does increase slightly above 300 Pa. It continues to behave as a Newtonian liquid at all temperatures. At 2.0 mol% P_2O_5 at 950 °C (Figure S1) the data shows little difference from 1.0 mol% P_2O_5 , exhibiting Newtonian behaviour at

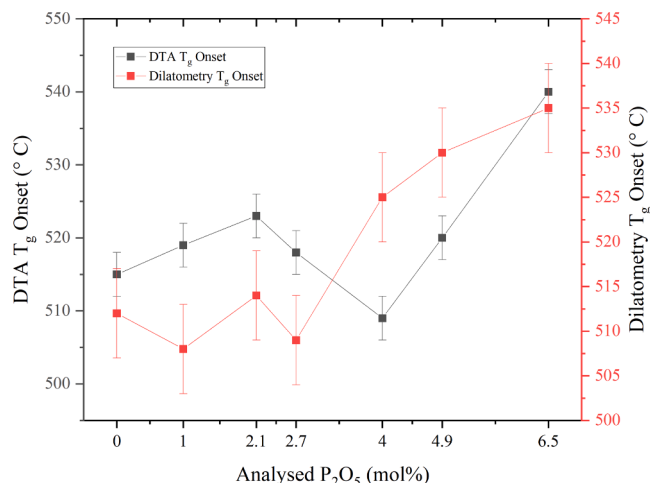


Fig. 13. DTA and dilatometric T_g onset temperatures as functions of analysed P_2O_5 content

Table 4

Experimental DTA and dilatometry thermal properties.

Sample	DTA T_g onset (°C)	DTA T_g Mid-point (°C)	Dilatometry T_g onset (°C)	Dilatometry T_g Mid-point (°C)	T_d (°C)	Coefficient of Thermal Expansion (CTE) ($1/T$) K
NBSP0.0	515 ± 3	532 ± 3	512 ± 5	532 ± 5	550 ± 5	$6.96 \pm 0.2 \times 10^{-6}$
NBSP1.0	519 ± 3	537 ± 3	508 ± 5	535 ± 5	550 ± 5	$6.88 \pm 0.2 \times 10^{-6}$
NBSP2.0	523 ± 3	540 ± 3	514 ± 5	545 ± 5	551 ± 5	$7.05 \pm 0.2 \times 10^{-6}$
NBSP3.0	518 ± 3	536 ± 3	509 ± 5	539 ± 5	550 ± 5	$6.59 \pm 0.2 \times 10^{-6}$
NBSP4.0	509 ± 3	540 ± 3	525 ± 5	561 ± 5	570 ± 5	$7.12 \pm 0.2 \times 10^{-6}$
NBSP5.0	520 ± 3	550 ± 3	530 ± 5	564 ± 5	575 ± 5	$7.30 \pm 0.2 \times 10^{-6}$
NBSP6.0	540 ± 3	562 ± 3	535 ± 5	569 ± 5	581 ± 5	$7.60 \pm 0.2 \times 10^{-6}$

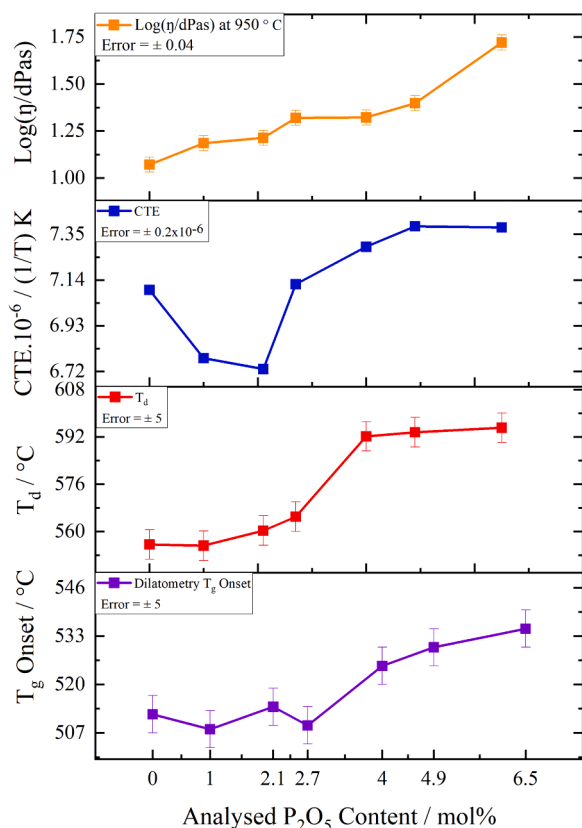


Fig. 14. Effects of increasing P_2O_5 content on viscosity at 950 °C, coefficient of thermal expansion, T_g onset, and T_d dilatometric softening point.

950 °C and the following temperatures (Figure S1-S4). At 3.0 mol% P_2O_5 (Figure S1-S4) the data show an increase in the shear stress, reading approximately 400 Pa, where it then reduces slightly when the rate decreases, demonstrating slightly non-Newtonian behaviour. At 4.0 mol% P_2O_5 the melt viscosity decreases in shear stress from approximately 400 Pa to 20 Pa between 950 and 1250 °C (Figures S1-S4), with some variance in the melt behaviour at 1050 °C, where there is strong evidence of non-Newtonian behaviour. The non-Newtonian behaviour is characterised by the slight hysteresis loop approximately between 10 and 15 s^{-1} , which has been identified to correspond to thixotropic behaviour, where the viscosity of the fluid is dependent on the time of shear rate, where viscosity decreases with time [77]. At 5.0 mol% P_2O_5 at 950 °C (Figure S1) the shear stress has a value of 500 Pa with variance in the Newtonian behaviour a 1250 °C (Figure S4). At 5.5 mol% P_2O_5 the shear stress increases to above 600 Pa with non-Newtonian behaviour being exhibited at 1150 °C, specifically thixoplastic behaviour (Figure S3). Finally, at 6.0 mol% P_2O_5 the shear stress at 950 °C increases to 1000 Pa with evidence of non-Newtonian behaviour, specifically thixoplastic behaviour, suggesting that as the P_2O_5 content increased the shear stress of the glass melts increased at 950 °C, corresponding to the increase in the viscosity.

Table 5

Viscosity of NBSP samples at different melting temperatures during heating cycle.

Temperature / (1/T) K	Log(η /dPas) \pm 0.04							
	NBSP0.0	NBSP1.0	NBSP2.0	NBSP3.0	NBSP4.0	NBSP5.0	NBSP5.5	NBSP6.0
8.18E-04	1.07151	1.18546	1.21373	1.32015	1.32222	1.39844	1.57466	1.72102
7.56E-04	0.55465	0.65677	0.66388	0.78199	0.75818	0.86162	0.91014	0.92495
7.03E-04	0.18931	0.28600	0.27684	0.37541	0.35740	0.43249	0.48891	0.46934
6.57E-04	-0.08495	-0.01185	-0.02384	0.04005	0.03161	0.07562	0.16423	0.14987

3.7. Structural analysis – Raman spectroscopy

3.7.1. Annealed and quenched NBSP samples

Figs. 16 and 17 show the Raman spectra of the annealed and quenched NBSP glasses, respectively. Tables 7 and 8 list the identified peaks in spectra for the annealed and quenched samples, and Table 9 lists the associations, according to literature, of the identified peaks. The spectra can be divided into three main regions: the low frequency region (200–800 cm^{-1}), the mid-frequency region (800–1200 cm^{-1}), and the high-frequency region (1200–1600 cm^{-1}). The low frequency region contains Raman bands that could be associated with either the breathing mode of B-O-Si(B) bonds from reedmergerite- and danburite-like rings that consist of $[SiO_2]$ and $[BO_4]$ tetrahedra in a mixed borosilicate phase; or the bending of ring-type metaborate groups, composed mainly from boron triangles [8,9,80,81], whilst the mid-frequency region has Raman bands associated with the symmetric stretch of Q^n species associated with the silicate network, and the high frequency region is associated with symmetric stretching of the borate network [13]. The samples are sodium borosilicate glasses, hence they contain two medium range sub-networks associated with silicate and borate, with sodium

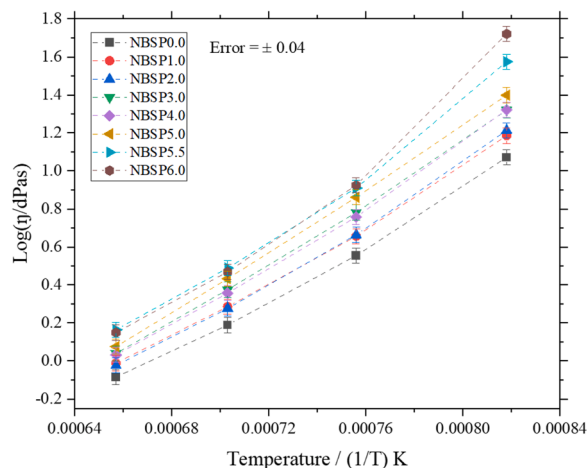


Fig. 15. Effects of temperature on log (viscosity) of NBSP samples at 8.18E-04 (1/T) K, 7.5E-04 (1/T) K, 7.03E-04 (1/T) K, and 6.5E-04 (1/T) K, with varying P_2O_5 content. The data is from a constant shear rate of 10 s^{-1} .

Table 6

Arrhenius parameters of the NBSP glass melts: Arrhenius activation energy (E_a / $KJ \cdot mol^{-1}$) and entropic factor of Arrhenius ($\ln(A_s / Pa \cdot s)$) as a function of P_2O_5 content.

Sample	E_a ($KJ \cdot mol^{-1}$)	$\ln(A_s / Pa \cdot s)$
NBSP0.0	16.429	-10.94
NBSP1.0	17.216	-11.42
NBSP2.0	17.815	-11.85
NBSP3.0	18.433	-12.08
NBSP4.0	18.541	-12.19
NBSP5.0	18.961	-12.32
NBSP5.5	20.242	-13.05
NBSP6.0	22.626	-14.74

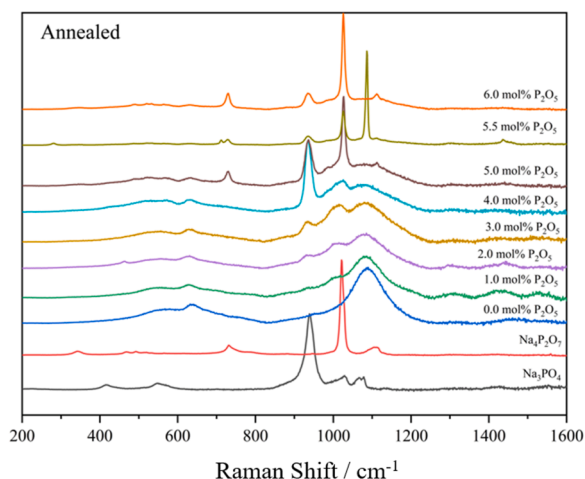


Fig. 16. Raman spectra of annealed NBSP glasses and sodium phosphate crystalline standards, Na_3PO_4 and $\text{Na}_4\text{P}_2\text{O}_7$.

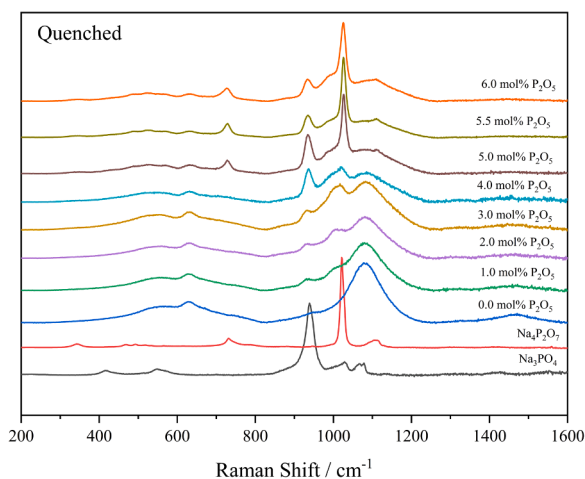


Fig. 17. Raman spectra of quenched NBSP glasses and sodium phosphate crystalline standards, Na_3PO_4 and $\text{Na}_4\text{P}_2\text{O}_7$.

Table 7
Raman peak maxima in the annealed NBSP glasses.

Sample	Raman spectral peak maxima (cm^{-1})
NBSP0.0	534, 630, 937, 1086, 1445
NBSP1.0	534, 630, 937, 1086, 1445
NBSP2.0	534, 630, 937, 1000, 1086, 1445
NBSP3.0	534, 630, 937, 1000, 1086, 1445
NBSP4.0	534, 630, 937, 1026, 1086, 1445
NBSP5.0	534, 630, 937, 990, 1026, 1086, 1109, 1445
NBSP5.5	534, 630, 729, 937, 990, 1026, 1086, 1109, 1445
NBSP6.0	630, 729, 937, 990, 1026, 1109, 1445
Na_3PO_4	416, 548, 939, 1022, 1066
$\text{Na}_4\text{P}_2\text{O}_7$	343, 733, 1022, 1111

cations acting as either modifier cations or charge compensators. The addition of P_2O_5 leads to the formation of a phosphate rich sub-network, where discrete PO_4^{3-} and $\text{P}_2\text{O}_7^{4-}$ species form outside of the silicate network [18]. Phosphorus scavenges metal cations and NBOs to charge compensate itself, leading to the re-polymerisation of the silicate network [18].

The base glass spectra for the annealed and quenched samples exhibited low intensity peaks at 495, 534/549, 630, and 729 cm^{-1} , an intense region between 800 and 1200 cm^{-1} with identified peaks at

Table 8
Raman peak maxima in the quenched NBSP glasses.

Sample	Raman spectral peak maxima (cm^{-1})
NBSP0.0	495, 549, 630, 935, 1000, 1078, 1472
NBSP1.0	495, 549, 630, 935, 1000, 1078, 1472
NBSP2.0	495, 549, 630, 935, 1000, 1078, 1472
NBSP3.0	495, 549, 630, 935, 1000, 1078, 1472
NBSP4.0	495, 549, 630, 935, 1000, 1078, 1472
NBSP5.0	495, 549, 630, 729, 935, 1000, 1026, 1078, 1111, 1472
NBSP5.5	495, 549, 630, 729, 935, 1000, 1026, 1078, 1111, 1472
NBSP6.0	495, 549, 630, 729, 935, 1000, 1026, 1078, 1111, 1472

Table 9
Raman peak maxima with associated referenced assignments for the annealed and quenched NBSP samples.

Raman shift (cm^{-1})	Attribution	Reference
534 (annealed)	Symmetrical stretching and partial deformation vibrations of Si-O-Si bridges	[49,127]
549 (quenched)	Breathing mode of B-O-Si(B) in reedmergnite- and/or danburite-like rings with Na_2O instead of CaO as a charge compensator for $^{(4)}\text{B}^{3+}$ units	[80,82–84, 127]
629 (annealed)	Metaborate vibrations of the ring-type	
628 (quenched)	Symmetric stretching of P-O-P	[80]
729 (annealed and quenched)	P-O stretching in PO_4^{3-} tetrahedra	[44,80, 85–87,114]
935 (quenched)	P-O stretching in $\text{P}_2\text{O}_7^{4-}$	[27,44,94]
1000 (annealed and quenched)	P-O symmetric stretching vibrations of pyrophosphate ($\text{P}_2\text{O}_7^{4-}$) Q^1 units	[88–90,114]
1026 (annealed and quenched)	Stretching of the NBO of the Q^3 structural units in silicate groups	[49,127]
1086 (annealed) / 1078 (quenched)	P-O stretching in $\text{P}_{(\text{IB})}^2$	[91]
1111 (quenched)	PO_2 vibrations of $\text{P}^{(2)}$ units connected to two borons ($\text{P}_{(\text{IB})}^2$) and PO_3 vibrations of $\text{P}^{(1)}$ species	[92]
1109 (annealed)	Si-O ⁻ stretching in Q^3 units	[84]
1445 (annealed)	BO_3 units with one bridging bond of BO_4 tetrahedra	[93]
1472 (quenched)	B-O(NBO) stretch	[82]

935/937, 1000, 1026, 1075/1079, 1086, and 1109/1111 cm^{-1} , and a broader, low intensity region between 1200 and 1600 cm^{-1} with identifiable peaks at 1315, 1330, 1469, and 1471 cm^{-1} .

When 0.0–3.0 mol% P_2O_5 was present in the annealed glasses, the peaks at 534 and 630 cm^{-1} increased in intensity before continuing to decrease in intensity upon further additions of P_2O_5 (4.0–6.0 mol%). As these peak intensities decreased, a peak at 729 cm^{-1} occurred at 5.0 mol% P_2O_5 and continued to increase in intensity to 6.0 mol% P_2O_5 . The band at 935 cm^{-1} increased in relative intensity between 0.0 and 3.0 mol% P_2O_5 , but reduced at 4.0 mol% P_2O_5 , then increasing to its highest relative intensity at 5.0 mol% P_2O_5 , before decreasing again at 5.5 mol% P_2O_5 . The peak at 1000 cm^{-1} was present at 2.0 and 4.0 mol% P_2O_5 and decreased in relative intensity upon additions of ≥ 5.0 mol% P_2O_5 at the expense of the peak at 1026 cm^{-1} . The broad band with a peak at ~ 1076 cm^{-1} increased in intensity between 1.0 and 4.0 mol% P_2O_5 , but then decreased at 5.0 mol% P_2O_5 , after which there was a sharp peak at ~ 1086 cm^{-1} , which then completely decreased again at 6.0 mol% P_2O_5 . The peak at 1109 cm^{-1} only occurred in samples with ≥ 5.0 mol% P_2O_5 and its relative intensity did not fluctuate greatly with increasing P_2O_5 content. In the high frequency region (1200–1600 cm^{-1}), the base glass spectrum exhibited two peaks centred at 1315 and 1471 cm^{-1} , where the additions of 1.0 mol% P_2O_5 saw the development of a third peak at ~ 1531 cm^{-1} . This peak shifted to higher and then lower frequencies upon the addition of 2.0 and 3.0 mol% P_2O_5 , respectively. At 4.0 mol% P_2O_5 , there were only two identifiable peaks centred at ~ 1311 and 1419 cm^{-1} . When 5.0–6.0 mol% P_2O_5 was present in the sample, there were still two peaks present, however, the peak that at ~ 1419 cm^{-1} was

replaced by a peak at $\sim 1432\text{ cm}^{-1}$.

For the quenched glasses, as the P_2O_5 content increased the Raman bands at 495 and 549 cm^{-1} decreased in their relative intensities, whilst the peak at 630 cm^{-1} increased until $3.0\text{ mol}\%$ P_2O_5 , before continuing to reduce in intensity from $4.0\text{ mol}\%$ P_2O_5 upwards. The peak at 729 cm^{-1} occurred from $5.0\text{ mol}\%$ P_2O_5 upwards, increasing in intensity with increasing P_2O_5 content. The peak at 935 cm^{-1} increased in relative intensity between 0.0 and $5.0\text{ mol}\%$ P_2O_5 , before decreasing at 5.5 and $6.0\text{ mol}\%$ P_2O_5 . The band at 1000 cm^{-1} was present in spectra for the 2.0 and $4.0\text{ mol}\%$ P_2O_5 samples, then it decreased in intensity at the expense of the peak at 1026 cm^{-1} upon additions of $\geq 5.0\text{ mol}\%$ P_2O_5 . The broad peak at 1078 cm^{-1} decreased in intensity whilst the peak at 1026 cm^{-1} increased, with increasing P_2O_5 content. In the high frequency region ($1200\text{--}1600\text{ cm}^{-1}$), two discernible peaks were identified, where the second peak moved to a lower frequency upon the addition of P_2O_5 .

3.7.2. Raman difference spectra

Fig. 18 shows the Raman difference spectra (RDS) of the annealed NBSP samples, with Table 10 listing the key intensities and likely associations based on literature. The RDS are produced by subtracting the Raman spectrum for the base glass that is common to all the samples i.e., sodium borosilicate glass with $0.0\text{ mol}\%$ P_2O_5 , from the spectra for the other samples that contain P_2O_5 , thereby presenting the effects of P_2O_5 additions in the y-axis. However, it should be noted that there are contributions from borate and silicate species, but these are being convoluted by the phosphate-specific intensities, hence other techniques such as MAS-NMR would be needed to establish the Q^n speciation of the borate and silicate units.

4. Discussion

4.1. X-ray diffraction

As the P_2O_5 contents of the samples increased, they became increasingly crystalline, with a change in the nature of the phosphate phases present. At lower P_2O_5 concentrations there were orthophosphate Q_0^0 species, $[\text{PO}_4]^{3-}$, as indicated by the Na_3PO_4 phase in the NBSP 4.0 sample. In sample NBSP $5.0\text{--}6.0$ there were Na_3PO_4 and $\text{Na}_4\text{P}_2\text{O}_7$ present, which introduced Q_1^1 pyrophosphate anions, $[\text{P}_2\text{O}_7]^{4-}$. However, the characteristic Bragg peaks associated with $\text{Na}_4\text{P}_2\text{O}_7$ occurred along with Na_3PO_4 , increasing in relative intensity with increasing P_2O_5 content. The crystallisation of Na_3PO_4 and $\text{Na}_4\text{P}_2\text{O}_7$ is consistent with results for other relevant glasses in which Na_2O is present at high levels ($> 20\text{ mol}\%$) [34,96]. Therefore, as the P_2O_5 content increases, the ratio

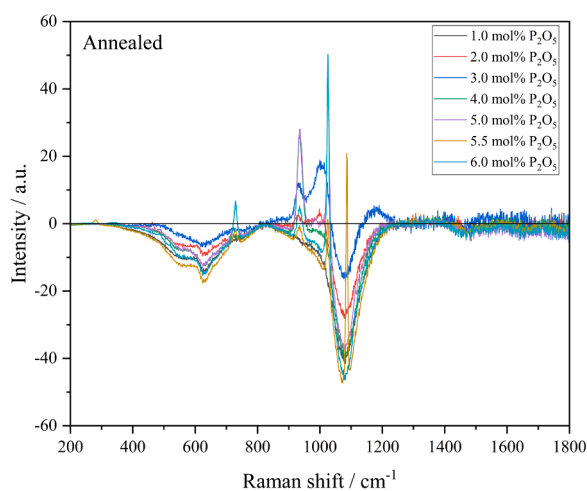


Fig. 18. Raman Difference Spectra (RDS) obtained by subtracting the Raman spectrum for sample NBSP 0.0 (base glass) from the Raman spectra of the other NBSP samples (NBSP 1.0 to 6.0).

Table 10

Raman peak maxima with associated referenced assignments.

Raman Intensity, cm^{-1}	Assignment	Reference
729	Symmetric stretching of P-O-P	[80,89]
937	P-O stretching in PO_4^{3-} Q^0 tetrahedra	[8,9,56,80,114,126]
1000	P-O stretching in $\text{P}_2\text{O}_7^{4-}$	[26,27,56,94,114]
1026	P-O symmetric stretching vibration of pyrophosphate Q^1 units Asymmetric stretching modes of Si-O- NBO Asymmetric stretching of PO^3	[90,93,95,63]
1109	P-O stretching in $\text{P}_{(\text{IB})}^2$	[91,92]
1445	BO_3 units with one bridging bond of BO_4 tetrahedra	[93]

of PO_4^{3-} to $\text{P}_2\text{O}_7^{4-}$ anions changes in favour of the pyrophosphate cations ($\text{P}_2\text{O}_7^{4-}$). However, this increase means that more Na^+ ions are needed to charge compensate the P^{5+} anions, resulting in the increase in the ratio of 3-coordinated boron ($^{[3]}\text{B}^{3+}$) to 4-coordinated boron ($^{[4]}\text{B}^{3+}$), and the subsequent increase in the degree of polymerization of the silicate network through the conversion of NBOs to BOs [9,31,34]. If this were the case, T_g could be expected to change. The transition of orthophosphate to pyrophosphate with increasing P_2O_5 content is, therefore, attributed to the clustering observed as the sodium phosphate crystal phases where the ratio of orthophosphate to pyrophosphate increases with increasing P_2O_5 content; this was the case for both the quenched and annealed glasses.

XRD was conducted on both annealed and quenched samples to understand whether annealing the samples had any effect on the crystalline phases in comparison to air quenching. The quenched samples presented cristobalite in samples NBSP 5.0, 5.5, and 6.0, while the annealed samples only presented cristobalite in sample NBSP 5.5. Having cristobalite present in the annealed NBSP 5.5 sample suggests that there was a small amount of unmelted silica in the glass arising from imperfect melting of the raw materials, meaning that the glass may have needed to be heated at either a higher temperature and/or left to dwell longer during melting to ensure all batched silica had been incorporated into the melt. The presence of SiO_2 in the quenched samples also indicates that the point at which the glass was poured had an impact on the crystallisation behaviour.

Glasses are non-equilibrium states of matter and move towards their equilibrium state when heated at a temperature below T_g . This phenomenon, which changes the glass properties, is referred to as structural relaxation [97]. During annealing, structural relaxation occurs, thermal stresses are removed, and the enthalpy of the glass reduces [98]. Hence, the glasses were annealed at $500\text{ }^\circ\text{C}$ because this is the temperature just below the T_g , where literature showed that the T_g of the base glass was expected to be approximately $515\text{ }^\circ\text{C}$ [103]. The annealed samples have a lower threshold because the annealing process had a slower cooling rate, where the structural relaxation of the glass subsequently leads to the nucleation and growth of crystals and/or phase separated droplets [99].

The heat treatment/thermal history of the glasses, whether annealed or quenched, has influenced the crystallisation behaviour, where the quenched glasses have X-ray measurable crystalline peaks at $5.0\text{ mol}\%$ P_2O_5 as opposed to at $4.0\text{ mol}\%$ P_2O_5 in the annealed glasses. Heat treatment (annealing) of a glass melt/matrix can have an effect on nucleation and crystallisation processes, where cooling at a constant rate or holding at a given temperature, in this case $500\text{ }^\circ\text{C}$, can enable any nuclei present in the melt/matrix to grow until they have reached a critical size, at which point they are retained and allowed to develop, resulting in their precipitation as crystals [100–102]. For example, formation and growth of a second, initially amorphous, phase and its growth during initial cooling of the melt and then heat treatment (annealing) at $500\text{ }^\circ\text{C}$ is consistent with heating at temperatures above

the T_g of this second phase (theoretical $T_g \sim 424$ °C based on the extrapolation of the nominal composition $75\text{Na}_2\text{O}-25\text{P}_2\text{O}_5$ mol% (obtained from XRD showing Na_3PO_4 as the first crystalline phase that forms, and calculated for the 4.0 mol% P_2O_5 sample from the SciGlass software database)) which has consequently placed the sample in a temperature regime (above T_g) whereby this second amorphous phase is capable of crystallisation. This could explain the presence of crystalline sodium phosphate (Na_3PO_4) at lower nominal P_2O_5 contents in the annealed (heat treated) glass samples compared to the quenched (unannealed and thus not heat treated) equivalent samples. This is an important finding as it illustrates the need for caution when investigating phase separation in glasses. It should also be noted that the cooling rate and temperature distribution of the quenched glasses are unknown, which could better inform the crystallisation behaviour. However, some literature on broadly similar sodium borosilicate glass systems has reported cooling rates, such as Yazawa et al. [104], Angeli et al. [83], and Peuket et al. [105] who reported the values 600 K/min, 0.7×10^6 K/min, and 3.0×10^4 K/min, respectively.

When the samples underwent the CCC heat treatment the sodium phosphate crystal phase transitions formed a cubic structure in samples NBSP 3.0, 4.0, and 5.0, to orthorhombic in samples NBSP 5.0 and 5.5, to hexagonal in sample NBSP 6.0. Interestingly, crystallinity occurred at a lower P_2O_5 content in the CCC regime heat treated glasses when compared to the annealed glasses, with X-ray crystallinity observed on a macroscale in the NBSP 4.0 sample and measurable in the NBSP 3.0 sample. These phases have developed because they are closer to their high-temperature equilibrium, meaning that during the HLW CCC heat treatment regime the samples were held at higher temperatures (e.g. >800 °C) for considerably longer, allowing the main phase nucleation sites to grow and crystallise [106].

Comparing the HLW CCC and LAW CCC NBSP glasses, both developed similar sodium phosphate crystalline phases with increasing P_2O_5 contents. The heat-treated samples demonstrated that the measurable solubility limit of P_2O_5 /onset of crystallization does differ with heating regime. The precipitation of the cristobalite and tridymite could decrease the chemical durability of the glasses because they strip SiO_2 from the glass matrix and thus can affect the rate of glass dissolution in water [106,107]. It should be noted that this data is limited in respect to the type and extent of crystallisation that the final Hanford glasses will exhibit, because of the reduced number of components in the studied glass system, and consequent differences in the overall composition. The P_2O_5 may interact and behave differently when in the presence of cations other than Na^+ , and with other glass formers and intermediates, such as Fe_2O_3 and Al_2O_3 . For example, a representative waste glass simulant composition reported by Achigar et al. [96], in the SiO_2 - B_2O_3 - Al_2O_3 - Fe_2O_3 - Na_2O - Li_2O - CaO glass system, exhibited two different crystal phases, NaCaPO_4 and NaLi_2PO_4 , where phosphate crystallisation occurred at 3.2 mol% P_2O_5 . Hence, the solubility limit of P_2O_5 and crystallisation behaviour strongly depend on glass composition and the abundance of each oxide present. However, the sodium borosilicate glass system studied here is still of relevance, given its wide use and application in common commercial applications, such as Pyrex-type glasses [15], in biomedical applications such as bone grafts [32], and as a common glass system used to represent and vitrify nuclear waste by countries such as the UK, USA, India, Japan and France [109]. A range of relevant literature has described the use of sodium borosilicate glasses to infer the behaviour and properties of full simulant wastes with respect to phosphorus additions, such as Krishnamurthy et al. [31], Schuller et al. [11], Rong et al. [109], and Munoz et al. [27,34].

4.2. Scanning electron microscopy (SEM)

The mixture of droplets observed in the SEM backscattered electron images (Figs. 9-12) may be indicative of liquid-liquid phase separation that may have occurred upon cooling, where one phase may have cooled before the other as the P_2O_5 content increased in the glass system. The

black and grey dots in the matrix of lighter grey may have been nucleation sites for crystals with potentially different compositions. However, the exact mechanism by which phase separation occurred is currently unknown i.e. whether spinodal decomposition, nucleation and growth, or both. Visual inspection of the morphology postulates that the phase separation took place via the nucleation and growth mechanism, where said mechanism occurred at low supersaturations, near to the immiscibility limit. However, conclusively stating that the phase separation occurred by the nucleation and growth mechanism cannot be undertaken, as it is notoriously difficult to determine the mechanism based solely on morphology. Craievich et al. [110] cited work by Seward et al. [111] who examined thin films of BaO-SiO_2 glass, reporting that compositions near the centre of the miscibility gap presented fine isolated droplets, however, at a later stage two interconnected phases were observed, indicating the intersecting growth when the composition was within the spinodal region. Vogel [15] reported that the high cation field strength of phosphorus allows it to dominate the process in mixed glass systems, such as $\text{Na}_2\text{O-B}_2\text{O}_3\text{-SiO}_2\text{-P}_2\text{O}_5$, where it gathers alkali cations from the unmixed borosilicate phase and into an additional phosphate rich droplet phase [45].

The relationship between crystallisation and liquid-liquid phase separation, or immiscibility, is subtle, however, it is generally accepted that the origin of immiscibility and crystallisation in silicate solutions derives from the thermodynamic driving force [112]. Studies by Uhlman [113] reported that local changes in the composition caused by phase separation phases:

- (i) Can increase or decrease the thermodynamic driving forces of crystallisation;
- (ii) Can enhance crystal nucleation through the existence of interfaces in the phase separated regions;
- (iii) This results in one of the liquid phases having a higher atomic mobility than the present homogeneous phase;
- (iv) This provides a larger driving force for the nucleation or atomic mobility by the interfacial regions between the enriched separated component in one of the phases.

It should be noted that crystallisation itself is a two-step process: (i) the initial nucleation of the crystal followed by (ii) the growth of the nuclei by the addition of more atoms [101]. There are also two types of nucleation: heterogeneous and homogeneous. The first occurs when the nuclei form at an already pre-existing surface or interface, and the latter occurs when nuclei form spontaneously in the melt/matrix [101]. When the crystals are small the positive surface energy term is dominant, making them unfavourable and re-dissolving back into the glass matrix [52,50]. When these crystals are larger than the critical nuclear size, the bulk free energy dominates instead, meaning the nuclei are stable and grow in size [101]. In heterogeneous nucleation, the crystal forms on an existing interface/surface, while in homogeneous nucleation the interface that is being formed is between the melt/matrix and crystal [101]. As a result, the combination of creating and eliminating interfaces leads to a reduction in the activation energy needed for crystallisation. Hence, heterogeneous nucleation is faster than homogeneous nucleation. Therefore, systems with more pre-existing interfaces such as phase separation, voids and crystals will have a higher nucleation rate than a glass system without such interfaces [101]. In summary, SEM has confirmed that the solubility limit of P_2O_5 in these glasses is between 2.7–4.0 mol% P_2O_5 , which is consistent with the XRD patterns (Fig. 4).

4.3. Thermal parameters

4.3.1. T_g , CTE, and T_d

The decrease of the T_g onset at 2.7 mol% P_2O_5 in the DTA data may suggest that the silicate network is becoming de-polymerised, resulting in an increase in NBOs in the glass network, and therefore, there may be more planar trigonal borate units in the system and that P_2O_5 may be

promoting the formation of P-O-B species leading to a less connected network and, therefore, a decrease in T_g [18]. There is not enough Na^+ ions to charge compensate the less polymerised phosphate units, hence the bonding of phosphate to a borate unit to form borophosphate species [18]. However, to establish whether this is the case, ^{31}P -NMR and ^{11}B -NMR would be required. Moreover, there is a difference in behaviour observed between the DTA and dilatometry-measured samples.

T_g is sensitive to the degree of network connectivity in the glass system, and the increase in NBOs in the silicate network decreases it, but the conversion of planar trigonal ^{3}B to tetrahedral ^{4}B units increases T_g [19,23]. Between 0.0 to 2.1 mol% P_2O_5 the T_g increased then reduced at 2.7 mol%, before continuing to increase again up to 6.5 mol% P_2O_5 . This observed behaviour of the dual effect of P_2O_5 has been observed previously by other researchers such as Cheng [114], who reported that for borosilicate glasses with the addition of 1.0 mol% P_2O_5 , T_g increased but after further additions T_g gradually decreased until the glass phase separated. The initial increase in T_g suggests this is a result of the increased polymerization of the silicate network, and that changes in the degree of polymerisation of the network upon further additions of P_2O_5 are due to the NBOs and metal cations being scavenged to charge compensate the phosphate specific species in the glass network [18]. The decrease in T_g in the DTA data may be evidence of the (in this case) negative effect of P_2O_5 , where there are not enough excess alkali cations to charge compensate the less polymerized PO_4^{3-} and $\text{P}_2\text{O}_7^{4-}$ units, and they instead form P-O-B linkages, however, the presence of the units needs to be confirmed using MAS-NMR [19,23]. O'Donnell et al. [52] reported that P_2O_5 had this dual effect on bioactive glasses, stating that when the P_2O_5 content was increased, instead of the T_g increasing as expected, it decreased which contradicted the theory. They then commented on phosphate additions needing to be charge balanced by modifier cations such as sodium and calcium, which are taken from the silicate network [52].

CTE can give qualitative information on glass structure, since CTE depends on the glass composition, thermal history and temperature range of the dilatometry data from which it is extracted. The presence of asymmetrical units in the glass structure will lead to an increase in the CTE because they will cause anharmonic vibrations, while a more symmetrical network would lead to a decrease in the CTE [115]. In Fig. 9, the increase in the CTE between 2.0 and 3.0 mol% P_2O_5 and 2.7 and 4.0 mol% P_2O_5 may be indicative of the network de-polymerising due to the formation of "less-symmetrical units" such as pentaborate (P-O-B) and triborate (^{3}B) groups, which in turn indicates an increase in NBOs present in the glass structure [115]. Studies by Klyuev [115] concluded, firstly, that if the CTE increased, it was because there was an increase in the abundance of NBOs. Secondly, that the glass network contained cations whose coordination numbers were changing within the temperature range that exceeded the lower T_g range; and lastly, that the glass structure contained layered or chain fragments that were linked together by Van der Waals bonds [116]. Therefore, there could be several reasons as to why the CTE increased in the dilatometry data. Minamf & Mackenzie [116] commented that a decrease in the cationic field strength led to the observed increase in CTE, because the CTE is controlled by the interactions between the cation and NBOs, hence the de-polymerisation of the glass network [116]. Both Munoz et al. [34] and Kirkpatrick and Brow [117] reported that P^{5+} attracts Na^+ cations from the silicate sub-network, resulting in its subsequent re-polymerisation [117,118]. This structural change may then result in effects on thermal properties and chemical durability.

Based on the available data, it can be shown that the T_d is following a broadly similar trend to T_g onset, in that it is steadily rising with increased P_2O_5 content. The softening temperature ranges between 0.0 to 2.7 mol% P_2O_5 and 4.0 to 6.5 mol% P_2O_5 are the same within uncertainties, however, there is a notable increase between 2.7 and 4.0 mol% P_2O_5 . In phase separated glasses, the softening of the glass determines the value of T_d , which is controlled by the more viscous phase. If that phase is continuous, then the shift to a higher temperature controlled by

the continuous high temperature phase [119]. According to Keyvani et al. [118], the increase in T_g and T_d is a result of the increase in the viscosity. Therefore, this suggests that the glasses have begun to phase separate between 2.7 and 4.0 mol% P_2O_5 which affects T_d .

4.4. High temperature viscosity (HTV)

The viscosity of fluids is a measurement of the its resistance to shear deformation, where the viscosity-temperature relationships determine the melting parameters, annealing temperatures, refining rate, and crystallization rate [120]. Viscosity directly dictates the relaxation processes in amorphous materials, and is reliant on the glass composition [120]. In this particular study, the experimental viscosity data will contribute to property-composition relationship models that provide potential glass compositions for application at the Hanford Waste Treatment and Immobilisation Plant and for waste streams high in P_2O_5 [121]. Previous authors have highlighted the importance of measuring the viscosity of glass melts to better inform not just processing properties, but to provide further information on a glasses' thermal properties such as T_g , and its structure [120,122,123], especially as changes in the composition which may reduce structural connectivity reduce the melt viscosity and vice versa [124].

A fluid's viscosity behaviour can be described as being Newtonian, which is characterised by the linear relationship between the applied shear stress and rate of shear, demonstrated in (2) [125]:

$$\sigma_{yx} = F/A = \eta Y_{yx} \quad (2)$$

Where σ is the shear stress, which is defined as the applied force, F , acting over a given unit area, A . The shear viscosity, η , is defined as the coefficient of proportionality between the shear rate and shear stress, whilst the shear strain, Y , is defined as the displacement gradient across the sample.

When the viscosity of fluid is not constant at a given temperature but instead relies on the rate of shear, the fluid is non-Newtonian. Non-Newtonian fluids can be grouped into three main categories [125]:

1. Systems where the value of Y at a certain point within the fluid is determined by the current value of σ : these substances are known as purely viscous, generalised Newtonian fluids (GNF) or time-dependent.
2. Systems where the relationship between σ and Y show further dependence on the duration of shear and the kinematic history are known as time-dependent-fluids.
3. Systems that exhibit a mixture of viscous fluid behaviour and of an elastic solid-like behaviour, for example a class of materials that show partial elastic recovery, creep recoil etc. These are visco-elastic or elastic-viscous fluids.

Reviewing the viscosity of the glass melts it can be determined that samples NBSP 1.0 to NBSP 3.0 and NBSP 5.0 behaved entirely as Newtonian fluids at temperatures 950 °C, 1050 °C, 1150 °C, and 1250 °C, but samples NBSP 0.0, NBSP 4.0, NBSP 5.5, and NBSP 6.0 acted as non-Newtonian fluids depending on the temperature, and may in fact have been type-two non-Newtonian fluids, 'time-dependent fluids', which show further dependence on the duration of shear and the kinematic history; or type-3, which is a mixture of viscous fluid behaviour and an elastic-solid-like behaviour [126]. However, the viscosity of the samples may have increased at higher P_2O_5 content at the expected Hanford Site melting temperature of 1150 °C, the majority of the samples still displayed Newtonian behaviour except for NBSP 0.0 and NBSP 5.5.

It should be noted that phase separated systems under shear flow can have anisotropic morphological evolution, which can even induce ordering of the structure [11]. Zhang et al. [11] found that in a binary system in which phase separation has occurred, the viscous phase is the minor phase and the viscosity of the bulk contribution differs from that

of the interfacial contribution, leading to a reduction on the non-Newtonian behaviour [11]. When this viscous phase is the major phase, the bulk concentration is comparable to that of the interfacial contribution and hence the non-Newtonian behaviour is instead strengthened [12].

The differences in viscous flow observed here have most likely come from the differences in the local molecular environments around that of the flow species in the glass melt [64]. Simmons et al. [64] proposed a model that was based on the concept that the shear structural relaxation processes which control viscosity are dependent on the size and type of microstructure(s) present in the glass melt [64]. If the system has an interconnected microstructure with different viscosities, then there are three types of viscosity behaviour that will follow, depending on the microstructure size [64]. When there are small microstructures due to a space averaging within the relative size, this can lead to the molecules having their activation energies and relaxation times equivalent to each other, and therefore, the distributions are small, with expected viscosity behaviour. However, as the microstructure grows, the areas in the microstructure will differ leading to non-equivalent activation energies and relaxation times [64]. This broadening of the distribution of molecules and increase in viscosity are accentuated as the relative size grows [64].

Therefore, considering this information and reviewing the viscosity results for the NBSP sample glass melts, the increase in viscosity may be a result, first of phase separation induced by the increase of the P_2O_5 content, and then with decreasing temperature, the presence of solid sodium phosphate crystalline phases acting as the major viscous phase, with the bulk concentration being comparable to the interfacial contribution, and hence the non-Newtonian behaviour of the melt.

4.5. Raman spectroscopy

The small band at 495 cm^{-1} could be associated with the vibrationally isolated Si-O-Si or Si-O-B mode of four-membered rings or SiO_4 tetrahedra with four BO ions [126]. The bands at $534/549\text{ cm}^{-1}$ have been attributed to the symmetrical stretching and partial deformation vibrations of Si-O-Si bridges [127,49]. The band at 630 cm^{-1} , according to literature, is potentially caused by the breathing mode of B-O-Si(B) in reedmergnerite- and/or danburite- like rings with Na^+ ions instead of a Ca^{2+} ions acting as charge compensators for $[4]B^{3+}$ units [80,82–84], or by metaborate vibrations of the ring-type [127]. The band at 729 cm^{-1} has been attributed to the symmetric stretching of P-O-P [80] and occurs from 5.0 mol% P_2O_5 upwards in both the annealed and quenched samples and can be matched to the same peak in the $Na_4P_2O_7$ crystalline standard. The band at $935/937\text{ cm}^{-1}$ can be assigned to the formation of the stretching of a Q_0^0 unit, which is consistent with the peak in the Na_3PO_4 crystal standard spectrum [44,80,85–87]. The bands at 1000 and 1026 cm^{-1} can be attributed to P-O symmetric stretching vibrations of the pyrophosphate Q_1^1 unit [42,44,88–90,94,114]. The bands at 1078 cm^{-1} and 1086 cm^{-1} are in the region where Q^3 units are expected, and so have been assigned to the stretching of the NBO of the Q^3 structural units in the silicate groups [38,80]. The bands at $1109/1111\text{ cm}^{-1}$ have been attributed to the combination of P-O stretching in $P_{(1B)}^2$ [116], PO_2 vibrations of $P^{(2)}$ units connected to two borons $P_{(1B)}^2$ and PO_3 vibrations of $P^{(1)}$ species [92], and Si-O⁻ stretching in Q^3 units [117]. The peaks centred at $\sim 1311/1315/1330$ and $1453/1469/1471\text{ cm}^{-1}$ could be attributed to loose $[3]B^{3+}$ units and $[3]B^{3+}$ units linked to $[3]B^{3+}$ units, respectively, whilst the peak at 1419 cm^{-1} can be attributed to $[3]B^{3+}$ units linked to $[4]B^{3+}$ units, and the peak at 1432 cm^{-1} can be attributed to $[3]B^{3+}$ units linked to boroxol rings [82,93].

The presence of the band at 630 cm^{-1} (reedmergnerite- and/or danburite- like rings) in both sets of glasses implies that the silicate and borate sub-networks are interconnected to some degree, but that the reduction in its intensity suggests that with increasing P_2O_5 content the silicate sub-network is re-polymerising and the borate sub-network is forming fewer Si-O-B linkages. The increase in the relative intensity of

the peak at 1026 cm^{-1} at the expense and reduction in the band at $\sim 1000\text{ cm}^{-1}$ suggests that there was an increase in the presence of pyrophosphate Q_1^1 units, which is supported by the presence of sodium phosphate crystals in the XRD pattern (Fig. 4) in samples with ≥ 5.0 mol % P_2O_5 . The broad band with peaks centred at $\sim 1076/1078\text{ cm}^{-1}$ decreased as the relative intensity at $1026/1086\text{ cm}^{-1}$ increased, suggesting that as the P_2O_5 content increased, there was an increase in the presence of Q_1^1 species at the expense of Q_{Si}^3 species. Overall, additions of P_2O_5 have the dual effect of de-polymerising and re-polymerising the silicate and borate networks by scavenging metal cations (Na^+) and NBOs.

4.5.1. Raman difference spectra

Detailed study of Raman spectroscopy data on various alkali and alkaline earth doped oxide glasses with similar glass formulations to the glasses in this study, have been reviewed to give details of the structural changes P_2O_5 can cause. Referring to the intensities produced by the RDS (Fig. 18), the 729 cm^{-1} intensity has been associated with the symmetric stretching of P-O-P bonds, whilst the 937 cm^{-1} intensity was associated with the symmetric stretching of the P-O bond isolated in $PO_4^{3-} Q^0$ tetrahedra [56,80,85,86,95,126]. However, Yadav et al. [80] instead associated the intensities at approximately 940 cm^{-1} with PO_2 symmetric stretching of NBOs in Q_0^1 units [80]. Litasov et al. [128] commented that the peak at 987 cm^{-1} could also be the symmetric stretching of P-O bonds in isolated PO_4^{3-} species, as also suggested by Mysen [56,57] and Trimble et al. [126]. When referring to the XRD patterns for the annealed NBSP samples (Fig. 4), orthophosphate and pyrophosphate species are present in the NBSP 4.0, 5.0, 5.5, and 6.0 samples, evidenced by the occurrence of sodium phosphate crystals. Therefore, it is reasonable to assume that the Raman band at 937 cm^{-1} has been caused by the symmetric stretching of the P-O bonds in isolated $PO_4^{3-} Q^0$ tetrahedra. The 729 cm^{-1} and 937 cm^{-1} intensities can be further supported by comparing them with the Na_3PO_4 and $Na_4P_2O_7$ crystal phase standard Raman spectra seen in Fig. 16, where the 729 cm^{-1} intensity is associated with $Na_4P_2O_7$ and 937 cm^{-1} with Na_3PO_4 . The intensity at $\sim 1000\text{ cm}^{-1}$ could either be attributed to the P-O bond stretching in $P_2O_7^{4-}$ or the stretching vibration of P-O bonds in the $P(Q^1)$ chain [56,57,80]. Support for this suggestion is evidenced by the occurrence of the pyrophosphate species as evidenced in the XRD patterns for samples NBSP 5.5 and 6.0 as sodium phosphate crystals (Fig. 4). The peak at 1026 cm^{-1} observed for samples NBSP 5.0, 5.5, and 6.0 could either be attributed to the asymmetric stretching modes of Si-O-NBO or the P-O symmetric stretching vibration of pyrophosphate Q_1^1 units [90,95]. However, this band only occurs in the amorphous-crystalline phase separated samples (samples NBSP 5.0 to 6.0). The 1026 cm^{-1} intensity is most likely the result of the P-O symmetric stretching vibration of the pyrophosphate Q_1^1 units in the sodium phosphate crystals, especially when compared with the $Na_4P_2O_7$ Raman spectrum, which has the characteristic peak at $\sim 1029\text{ cm}^{-1}$. The intensity at 1114 cm^{-1} observed for samples NBSP 5.0, 5.5 and 6.0 can be attributed to $Na_4P_2O_7$ when compared to the $Na_4P_2O_7$ Raman spectrum in Fig. 11. The intensity at 1109 cm^{-1} observed for samples NBSP 5.0, 5.5 and 6.0 may be attributed to P-O bond stretching in $P_{(1B)}^2$ units [91, 92]. The Raman intensity at 1445 cm^{-1} observed in all spectra, from samples NBSP 0.0 to 6.0, can be assigned to BO_3 units with one bridging bond of a BO_4 tetrahedron [93].

5. Conclusions

Increasing the P_2O_5 content in the annealed sodium borosilicate glass system studied here increased its susceptibility to immiscibility, where at 3.0 mol% the glass matrix was amorphous, but at ≥ 4.0 mol% there was evidence of nucleation-type phase separation, as evidenced by BS-SEM images, and the presence of sodium phosphate crystal phases, as determined by XRD patterns. The changes in composition were reflected in the structural analysis of the samples, where the Raman intensity

band at 630 cm^{-1} , representative of the reedmergnerite- and/or danburite- like rings, decreased in intensity with increasing P_2O_5 content, suggesting a change in the polymerisation of the silicate and borate sub-networks. This decrease in intensity suggested that the silicate network may have been re-polymerising through the conversion of NBOs to BOs, which then affected the thermal, rheological, and crystallisation behaviour. The T_g both increased and decreased with increasing P_2O_5 content, consistent with previous literature. The viscosity of the glass melts increased with increasing P_2O_5 content and decrease in temperature, where $\geq 4.0\text{ mol}\%$ resulted in non-Newtonian fluids. This change from Newtonian to non-Newtonian behaviour may have been a result of the nucleation-type phase separation, where the presence of solid sodium phosphate crystals were acting as the major viscous phase. The solubility of P_2O_5 and subsequent occurrence of sodium phosphate crystal phases was affected by the thermal history of the glass, i.e. annealed or quenched. When the glass melt was quenched, crystalline phases were not detected by XRD until $4.0 < \text{P}_2\text{O}_5 \leq 5.0\text{ mol}\%$. When the annealed quenched glasses underwent two different CCC heat treatments, they exhibited measurable crystalline phases at $3.0 < \text{P}_2\text{O}_5 \leq 4.0\text{ mol}\%$. This difference in the point at which measurable crystalline phases occur as a function of heat treatment, informs the understanding of the relationship between temperature and viscosity, which is paramount in determining the correct melting regime in glass production and processing. However, it has also revealed that the solubility limit of P_2O_5 could either be regarded as the point at which crystallisation occurs or the point at which homogeneous materials develop inhomogeneity at a measurable length scale. Therefore, this study is useful in guiding future development of more complex glass systems pertaining to radioactive waste streams rich in P_2O_5 , for example those from the Hanford Site.

CRedit authorship contribution statement

K.L. Skerratt-Love: Funding acquisition, Data curation, Writing – review & editing, Writing – original draft. **J.L. George:** Funding acquisition, Supervision. **A.M.T. Bell:** Funding acquisition, Writing – review & editing. **F. Sweeney:** Funding acquisition, Writing – review & editing. **D. Cutforth:** Funding acquisition. **C.E. Lonergan:** Conceptualization. **D.R. Dixon:** Supervision. **A.A. Kruger:** Supervision. **P.A. Bingham:** Writing – review & editing, Supervision.

Declaration of Competing Interest

The authors declare that they have no known competing financial interests or personal relationships that could have appeared to influence the work reported in this paper.

Data availability

The authors do not have permission to share data.

Funding acknowledgements

Funding is acknowledged from Sheffield Hallam University (SHU) and the US Department of Energy Office of River Protection (ORP). We also wish to acknowledge the Henry Royce Institute for Advanced Materials, funded through EPSRC grants EP/R00661X/1, EP/S019367/1, EP/P02470X/1 and EP/P025285/1, for Contour Elite access to the Renishaw CCD Camera Raman Spectrometer at Royce at the University of Sheffield.

Supplementary materials

Supplementary material associated with this article can be found, in the online version, at doi:[10.1016/j.jnoncrysol.2022.121999](https://doi.org/10.1016/j.jnoncrysol.2022.121999).

References

- [1] A. Goel, J.S. McCloy, R. Pokorny, A.A. Kruger, Challenges with vitrification of Hanford High-Level Waste (HLW) to borosilicate glass – an overview, *J. Non-Cryst. Solids: X* 4 (2019), 100033.
- [2] D. Dixon, C. Stewart, J. Venarsky, J. Peterson, G. Hall, T. Levitskaia, J. Allred, W. Eaton, J. Lang, M. Hall, D. Cutforth, A. Rovira, R. Peterson, Vitrification of Hanford Tank Waste 241-AP-107 in a Continuous Laboratory-Scale Melter, 0, Pacific Northwest National Laboratory, 2019. PNNL-28361Rev. <https://www.osti.gov/servlets/purl/1505629>.
- [3] J.D. Vienna, D.-S. Kim, D.C. Skorski, J. Matyas, Glass property models and constraints for estimating the glass to be produced at Hanford by implementing current advanced glass formulation efforts, PNNL-22631, Rev 1 (2013).
- [4] J. Vienna, G. Piepel, D. Kim, J. Crum and C. Lonergan, 2016 Update of Hanford glass property models and constraints for use in estimating the glass mass to be produced at Hanford by implementing current enhanced glass formulation efforts, PNNL-25835, (2016).
- [5] V. Gervasio, J. Vienna, D. Kim, A. Kruger, Impacts of process and prediction uncertainties on projected Hanford waste glass amount, PNNL-26996 EWG-RPT-015, Rev 0.0 (2018).
- [6] A.A. Kruger, D.-S. Kim, J.D. Vienna, Preliminary ILAW Formulation Algorithm Description, 24590 LAW RPT-RT-04-0003, Rev 1 (2013).
- [7] C.H. Delegard and S.A. Jones, Chemical Disposition of Plutonium in Hanford Site Tank Wastes, PNNL-23468-Rev.1, 1233488, (2015).
- [8] C.L. Hayward, The Vibrational Spectroscopy of Borate Minerals, PhD thesis, University College London, (1993). <https://discovery.ucl.ac.uk/id/eprint/10106244/1/out.pdf> (accessed January 1, 2022).
- [9] Z. Wang, L. Cheng, Structural evolution of CeO₂-doped alkali Boroaluminosilicate glass and the correlation with physical properties based on a revised structural parameter analysis, *RSC Adv.* 6 (2016) 5456–5465.
- [10] J.S. McCloy and J.D. Vienna, Glass composition constraint recommendations for use in life-cycle mission modeling, PNNL-19372, 978973, (2010).
- [11] S. Schuller, O. Pinet, A. Grandjean, T. Blisson, Phase separation and crystallization of phase separation and crystallization of borosilicate glass enriched in MoO₃, P₂O₅, ZrO₂, CaO, *J. Non Cryst. Solids* 354 (2008) 296–300.
- [12] J. Vienna, G. Piepel, D. Kim, J. Crum and C. Lonergan, 2016 Update of Hanford glass property models and constraints for use in estimating the glass mass to be produced at Hanford by implementing current enhanced glass formulation efforts, PNNL-25835, 2016.
- [13] P.A. Bingham, S. Vaishnav, S.D. Forster, A. Scrimshire, B. Jaganathan, J. Rohini, J.C. Marra, K.M. Fox, E.M. Pierce, P. Workman, J.D. Vienna, Modelling the sulfate capacity of simulated radioactive waste borosilicate glasses, *J. Alloys Compd.* 695 (2017) 656–667.
- [14] F.J. Ryerson, P.C. Hess, The role of P₂O₅ in silicate melts, *Geochim. Cosmochim. Acta* 44 (1979) 611–624.
- [15] W. Vogel, *Glass Chemistry*, 2nd edition, Springer-Verlag, 1965, p. 146.
- [16] S. Schuller, Chapter 4: Phase Separation in Glasses, *Glass to Crystal: Nucleation, Growth, and Phase Separation: from Research to Applications*, EDP Sciences, Les Ulis, 2017, pp. 125–154. <https://doi.org/10.1051/978-2-7598-1997-3.c011>.
- [17] J.D. Vienna & D. Kim, Preliminary IHLW Formulation Algorithm Description. (No. 24590-HLW-RPT-RT-05-001, Rev 0). River Protection Project, Hanford Tank Waste Treatment and Immobilization Plant, Richland, Washington (2008).
- [18] I.S. Muller, B. Dutta, C.F. Feng, F. Perez-Cardenas, H. Gan, I.L. Pegg, K. Hight, M. Laurenzi, S. Grant, T. Shatz, B. Bitner, C. Mooers, E. Malone, G. Bazemore, I. Carranza, L. Berger, L. Su, M. Timmons, S.T. Lai, Final Report: Glass Formulation And Testing With RPP-WTP LAW Simulants, VSL-01R3560-2, Rev. 0 (2016).
- [19] I.S. Muller, I.L. Pegg, H. Gan, A. Buechele, E. Rielley, G. Bazemore, R. Cecil, K. Hight, C. Mooers, T. Lai, A. Kruger, Final Report. Baseline LAW Glass Formulation Testing, VSL-03R3460-1, Rev (2015) 0.
- [20] A.A. Kruger, K.S. Matlack, Glass Formulation Testing To Increase Sulfate Incorporation - Final Report VSL-04R4960-1, Rev 0, 2/28/05, Vitreous State Laboratory, The Catholic University of American, Washington, D.C, 2012.
- [21] A.A. Kruger, I.L. Pegg, K.S. Matlack, I. Joseph, I.S. Muller, and W. Gong, Final Report - LAW Envelope C Glass Formulation Testing to Increase Waste Loading, VSL-05R5900-1 (2013).
- [22] A.A. Kruger, I.L. Pegg, K.S. Matlack, I. Joseph, I.S. Muller, W. Gong, Final Report - LAW Envelope A and B Glass Formulations Testing to Increase Waste Loading. VSL-06R6900-1, REV 0 (2006). ORP-56322.
- [23] A.A. Kruger, I.L. Pegg, K.S. Matlack, I. Joseph, I.S. Muller, and W. Gong, Final Report – Enhanced LAW Glass Formulation Testing, VSL-07R1130-1, Rev. 0, dated 10/05/07 ORP-56293 (2007).
- [24] A.A. Kruger, I.L. Pegg, K.S. Matlack, I. Joseph, I.S. Muller, W. Gong, Final Report - Glass Formulation Development and DM10 Melter Testing with ORP LAW Glasses, VSL-09R1510-2, Rev. 0 (2013) dated 6/12/09 ORP-56296.
- [25] A.A. Kruger, I.S. Muller, I. Joseph, K.S. Matlack, H. Gan, and I.L. Pegg, Waste Loading Enhancements For Hanford Law Glasses VLS-10R1790-1 FINAL REPORT REV 0 12/1/2010 ORP-48578 (2010).
- [26] H. Grussaute, L. Montagne, G. Palavit, J.L. Bernard, Phosphate speciation in Na₂O-CaO-P₂O₅-SiO₂ and Na₂O-TiO₂-P₂O₅-SiO₂ glasses, *J. Non Cryst. Solids* 263-264 (2000) 312–317.
- [27] F. Muñoz, Phosphate speciation in sodium borosilicate glasses studied by nuclear magnetic resonance, *J. Non Cryst. Solids* 352 (2006) 2958–2968.
- [28] M.J. Plodinec, Borosilicate glasses for nuclear waste immobilisation, *Glass Technol.* 41 (2000) 186–192.

- [29] M.J. Toplis, B. Reynard, Temperature and time-dependent changes of structure in phosphorus containing aluminosilicate liquids and glasses: in situ Raman spectroscopy at high temperature, *J. Non Cryst. Solids* 263-264 (2000) 123–131.
- [30] M.J. Toplis, D.B. Dingwell, The variable influence of P_2O_5 on the viscosity of melts of differing alkali/aluminum ratio: implications for the structural role of phosphorus in silicate melts, *Geochim. Cosmochim. Acta* 60 (1996) 4107–4121.
- [31] A. Krishnamurthy, T. Nguyen, M. Fayek, B. Shabaga, S. Kroeker, Network structure and dissolution properties of phosphate-doped borosilicate glasses, *J. Phys. Chem. C* 124 (38) (2020).
- [32] Y. Yu, B. Stevansson, M. Eden, Medium-Range Structural Organisation of Phosphorus-Bearing Borosilicate Glasses Revealed by Advanced Solid-State NMR Experiments and MD Simulations: consequences of B/Si Substitutions, *J. Phys. Chem. B* 121 (2017) 9737–9752.
- [33] M. Rinke and H. Eckert, The Mixed Network Former Effect in Glasses: Solid State NMR and XPS Structural Studies of the Glass System $(Na_2O)_x(BPO_4)_{1-x}$.
- [34] F. Muñoz, L. Montagne, L. Delevoeye, Influence of phosphorus speciation on the phase separation of $Na_2O-B_2O_3-SiO_2$ glasses, *Phys. Chem. Glasses* 49 (2008) 339–345. *Physical Chemistry Chemical Physics* 13 (2011) 6552–6565.
- [35] N. Stone-Weiss, H. Bradtmüller, M. Fortino, M. Bertani, R.E. Youngman, A. Pedone, H. Eckert, A. Goel, Combined experimental and computational approach toward the structural design of borosilicate-based bioactive glasses, *J. Phys. Chem. C* 124 (2020) 17655–17674.
- [36] M.M. Smedskaer, J.C. Mauro, R.E. Youngman, C.L. Hogue, M. Potuzak, Y. Yue, Topological principles of borosilicate glass chemistry, *J. Phys. Chem. B* 115 (44) (2011) 12930–12946, <https://doi.org/10.1021/jp208796b>.
- [37] G.M.S. Shafei, The Polarizing Power of Metal Cations in (Hydr)Oxides, *J. Colloid Interface Sci* 182 (1996) 249–253.
- [38] A. Takada, J. Parker, A. Durán, and K. Bange, Teaching Glass Better. International Commission on Glass (ICG), (2018).
- [39] J.E. Shelby, Introduction to Glass and Technology, 2nd Edition, The Royal Society of Chemistry, London, 2005.
- [40] R. Dupree, D. Holland, M.G. Mortuza, The role of small amounts of P_2O_5 in the structure of alkali disilicate glasses, *Phys. Chem. Glasses* 29 (1988) 18–21.
- [41] P. Lu, S. Kapoor, L. Kobera, J. Brus, A. Goel, Structural dependence of crystallization in phosphorus-containing sodium aluminoborosilicate glasses, *J. Am. Ceram. Soc.* 105 (2022) 2556–2574.
- [42] S. Liu, G. Li, Y. Yue, L. Hu, W. He, Effect of network modifiers on the opalescence and crystallization behavior of opal glasses, *Glass Technol.* 52 (2011) 67–72.
- [43] M.K. Murthy, Influence of platinum nucleation on constitution of and phase separation in sodium phosphate glasses, *J. Am. Ceram. Soc.* 44 (1961) 412–417.
- [44] P. Taylor, A review of phase separation in borosilicate glasses, with reference to nuclear fuel waste immobilization, Atomic Energy of Canada Limited (1990).
- [45] M.H. Langowski, The incorporation of P, S, Cr, F, Cl, I, Mn, Ti, U, and Bi into simulated nuclear waste glasses: literature study, PNNL-10980 (1996).
- [46] J.S. McCloy & J.D. Vienna, Glass Composition Constraint Recommendations for Use in Life-Cycle Mission Modeling, PNNL-19372, 978973 (2010).
- [47] J.D. Vienna, D.S. Kim, D.C. Skorski, J. Matyas, Glass Property Models and Constraints for Estimating the Glass to be Produced at Hanford by Implementing Current Advanced Glass Formulation Efforts, PNNL-22631, Rev.1 (2013).
- [48] A. Makishima, J.D. Mackenzie, J.J. Hammel, The leaching of phase-separated sodium borosilicate glasses, *J. Non Cryst. Solids* 31 (3) (1979) 377–383.
- [49] D.A. McKeown, I.S. Muller, A.C. Buechele, I.L. Pegg, C.A. Kendziora, Structural characterization of high-zirconia borosilicate glasses using Raman spectroscopy, *J. Non Cryst. Solids* 262 (2000) 126–134.
- [50] W. Vogel, Glass Chemistry, Springer-Verlag Berlin An, 2012.
- [51] W. Vogel, Structure and Crystallisation of Glasses, Elsevier Science, 2014.
- [52] D. O'Donnell, D.S.J. Watts, R.V. Law, R.G. Hill, Effect of phosphate content in two series of quaternary bioglasses on structure and properties studied by magic-angle-spinning nuclear magnetic resonance (MAS-NMR) spectroscopy—Part ii: physical properties, *J. Non Cryst. Solids* 354 (30) (2008) 3554–3560.
- [53] M. Fabian, Z. Kovacs, J.L. Labar, A. Sulyok, Z.E. Szekacs, V. Kovacs Kis, Network structure and thermal properties of bioactive $(SiO_2-CaO-Na_2O-P_2O_5)$ glasses, *J. Mater. Sci.* 55 (6) (2020) 2303–2320.
- [54] M. Soleimanzade, B.E. Yekta, V. Marghussian, Devitrification and Phase Separation of Zinc Borosilicate Glasses in the Presence of MgO, P_2O_5 , and ZrO_2 , *Int. J. Appl. Glass Sci.* 5 (2) (2014) 185–192.
- [55] M. Szumera, B. Lagowska, J. Sulowska, P. Jelen, Z. Olenjniczak, R. Lach, A. Berezicka, A. Kijo-Kleczkowska, Investigating the crystallization process of boron-bearing silicate-phosphate glasses by thermal and spectroscopic methods, *Molecules* 27 (3) (2022) 867.
- [56] B.O. Mysen, Phosphorus solubility mechanisms in haplogranitic aluminosilicate glass and melt: effect of temperature and aluminum content, *Contrib. Mineral. Petrol.* 133 (1998) 38–50.
- [57] B.O. Mysen, Phosphorus speciation changes across the glass transition in highly polymerized alkali silicate glasses and melts, *Am. Mineral.* 81 (1996) 1531–1534.
- [58] S. Liu, C. Zhu, Y. Zhang, Z. Xiao, Y. Yue, Composition dependence of spontaneous crystallisation of phosphosilicate glass melts during cooling, *Glass Technol.* 53 (2012) 235–239.
- [59] S.V. Mulevanov, N.I. Minko, S.A. Kemenov, Effect of adding phosphorus oxide on the dilatometric properties of silicate container glasses, *Glasses Ceram.* 64 (2007) 391–394.
- [60] P.A. Bingham, The effects of 1 wt% P_2O_5 addition on the properties of container glass, *Glass Technol.* 45 (2004) 255–258.
- [61] H.L. Giles, P.W. Hurley, H.W. Webster, Simple approach to the analysis of oxides, silicates and carbonates using X-ray fluorescence spectrometry, *X-Ray Spectrom.* 24 (1995) 205–218.
- [62] D.R. Neuville, B.O. Mysen, Role of aluminium in the silicate network: in situ, high-temperature study of glasses and melts on the join $SiO_2-NaAlO_2$, *Geochim. Cosmochim. Acta* 60 (1996) 1727–1737.
- [63] J. Marcial, O.K. Neill, M. Newville, J.V. Crum, J. McCloy, Effect of cooling profile on crystalline phases, oxidation state, and chemical partitioning of complex glasses, *MRS Adv.* 5 (2020) 1–11.
- [64] J.H. Simmons, S.A. Mills, B.F. Howell, Effect of Phase Separation On the Physical and Chemical Properties of Glasses-Density and Chemical Durability, National Bureau of Standards, 1974. NBSIR 74-510.
- [65] J.H. Christian, Crystallization in High-Level Waste Glass: a Review of Glass Theory and Noteworthy Literature, SRNL-STI-2015-004125, Rev 0 (2015).
- [66] C.E. Lonergan, J. Rice, C. Skidmore, M.J. Schweiger, P. Hrma, The effects of mixing multi-component HLW glasses on spinel crystal size, *J. Nucl. Mater.* 558 (2022), 153318.
- [67] D.L. McClane, J.W. Amoroso, K.M. Fox, A.A. Kruger, Nepheline crystallization behavior in simulated high-level waste glasses, *J. Non Cryst. Solids* 502 (2019) 215–224.
- [68] J.G. Reynolds, P. Hrma, The kinetics of spinel crystallization from a high-level waste glass, *MRS Proc.* 465 (1996) 65.
- [69] C.P. Rodriguez, J.S. McCloy, M.J. Schweiger, J.V. Crum, & A.E. Winschell, Optical basicity and nepheline crystallization in high alumina glasses, PNNL-20184, EMSP-RPT-003, 1019213 (2011).
- [70] V. Gervasio, J. Vienna, J. Lang, B. Westman, S. Sannoh, R. Russell, D. Kim, S. Cooley, J. George, D. Cutforth, S. Baird, Enhanced Hanford low-Activity Waste Glass Property Data development: Phase 4, Pacific Northwest National Laboratory, 2021. PNNL-31556.
- [71] R. Russell, Y.-S. Chou, B. McCarthy, L. Darnell, V. Gervasio, J. Mayer, J. Lang, S. Cooley, J. Vienna, G. Piepel and M. Schweiger, Glass compositions and properties of enhanced waste glass with high alumina content for high-level waste, EWG-RPT-013, Rev. 0.0, PNNL-27138, (2018).
- [72] J. Colombani, J. Bert, Toward a complete description of nucleation and growth in liquid-liquid phase separation, *J. NonEquilib. Thermodyn.* 29 (4) (2004), <https://doi.org/10.1515/JNETDY.2004.063>.
- [73] A. Messaâdi, N. Dhouiabi, H. Hamda, F. Belgacem, Y. Abdelkader, N. Ouerfelli, A. Hamzaoui, A. A New equation relating the viscosity Arrhenius temperature and the activation energy for some Newtonian classical solvents, *E-J. Chem.* (2015) 1–15.
- [74] P. Hrma, A.A. Kruger, High-temperature viscosity of many-component glass melts, *J. Non Cryst. Solids* 437 (2016) 17–25.
- [75] K. Gunasekera, S. Bhosle, P. Boolchand, M. Micoulaut, Superstrong nature of covalently bonded glass-forming liquids at select compositions, *J. Chem. Phys.* 139 (2013), 164511.
- [76] G. Ovarlez, Introduction to the rheometry of complex suspensions. Understanding Rheology of Concrete, Elsevier, 2012, pp. 23–62.
- [77] U. Eberhard, J. Hansjoerg, M. Florianic, P. Bertsch, J. Jiménez-Martínez, S. Andrade, M. Holzner, Determination of the Effective Viscosity of Non-Newtonian Fluids Flowing Through Porous Media, *Front. Phys.* 7 (2019).
- [78] C. Holmes, M. Cates, M. Fuchs, P. Sollich, Glass transitions and shear thickening suspension rheology, *J. Rheol. (N Y N Y)* 49 (1) (2005).
- [79] Z. Żolek-Tryznowska, 6-Rheology of printing inks, in: J. Izdebska, S. Thomas (Eds.), Printing polymers, Fundamentals and Applications, William Andrew Publishing, 2016, pp. 82–99.
- [80] A.K. Yadav, P. Singh, A review of the structures of oxide glasses by Raman spectroscopy, *RSC Adv.* 5 (2015) 67583–67609.
- [81] V. Jolivet, Quantification of boron in aluminoborosilicate glasses using Raman and ^{11}B NMR, *J. Non Cryst. Solids* 511 (2019) 50–61.
- [82] D. Möncke, G. Tricot, A. Winterstein-Beckmann, L. Wondraczek, E.I. Kamitsos, On the connectivity of borate tetrahedra in borate and borosilicate glasses, *Phys. Chem. Glasses* 56 (2015) 203–211.
- [83] F. Angeli, O. Villain, S. Schuller, T. Charpentier, D. de Ligny, L. Bressel, L. Wondraczek, Effect of temperature and thermal history on borosilicate glass structure, *Phys. Rev. B* 85 (2012), 054110.
- [84] D. Manara, A. Grandjean, D.R. Neuville, Advances in understanding the structure of borosilicate glasses: a Raman spectroscopy study, *Am. Mineral.* 94 (2009) 777–784.
- [85] H. Yamashita, H. Yoshino, K. Nagata, I. Yamaguchi, M. Ookawa, T. Maekawa, NMR and Raman Studies of $Na_2O-P_2O_5-SiO_2$ Glasses, *J. Ceram. Soc. Jpn.* 106 (1998) 539–544.
- [86] M.H. Manghni, A. Hushur, T. Sekine, J. Wu, J.F. Stebbins, Q. Williams, Raman, Brillouin, and nuclear magnetic resonance spectroscopic studies on shocked borosilicate glass, *J. Appl. Phys.* 109 (2011), 113509.
- [87] D.A. McKeown, A.C. Buechele, C. Viragh, I.L. Pegg, Raman and X-ray absorption spectroscopic studies of hydrothermally altered alkali-borosilicate nuclear waste glass, *J. Nucl. Mater.* 399 (2010) 13–25.
- [88] M.T. Rinke, H. Eckert, The mixed network former effect in glasses: solid state NMR and XPS structural studies of the glass system $(Na_2O)_x(BPO_4)_{1-x}$, *J. Phys. Chem. C* 111 (2011) 6552.
- [89] R. Y. J. Kalaiselvi, D. Shanmukaraj, B. Palanivel, S. Mohan, R. Murugan, Ionic conductivity and Raman investigations on the phase transformations of $Na_4P_2O_7$, *J. Alloys Compd.* 340 (2002) 6.
- [90] L. Giacomazzi, L. Martin-Samos, A. Alessi, N. Richard, A. Boukenter, Y. Ouerdane, S. Girard, M. Valant, S. De Gironcoli, $v-P_2O_5$ micro-clustering in P-doped silica studied by a first-principles Raman investigation, *Sci. Rep.* 9 (2019).
- [91] D. Raskar, M.T. Rinke, H. Eckert, The Mixed-Network Former Effect in Phosphate Glasses: NMR and XPS Studies of the Connectivity Distribution in the Glass System $(NaPO_3)_{1-x}(B_2O_3)_x$, *J. Phys. Chem. C* 112 (2008) 12530–12539.

- [92] D. Zieliński, C. Cramer, H. Eckert, Structure/Property Correlations in Ion-Conducting Mixed-Network Former Glasses: solid-State NMR Studies of the System $\text{Na}_2\text{O}-\text{B}_2\text{O}_3-\text{P}_2\text{O}_5$, *Chem. Mater.* 19 (2007) 3162–3170.
- [93] M. Seshadri, C. Batestin, L.L. Silva, M.J.V. Bell, V. Anjos, Effect of compositional changes on the structural properties of borophosphate glasses: ATR-FTIR and Raman spectroscopy, *Vib. Spectrosc.* 110 (2020), 103137.
- [94] P. Kiran, V. Ramakrishna, M. Trebbin, N.K. Udayashankar, H.D. Shashikala, Effective role of $\text{CaO}/\text{P}_2\text{O}_5$ ratio on $\text{SiO}_2\text{-CaO-P}_2\text{O}_5$ glass system, *J. Adv. Res.* 8 (3) (2017) 279–288.
- [95] R. Gangadharan, J. Kalaiselvi, D. Shanmukaraj, B. Palanivel, S. Mohan, R. Murugan, Ionic conductivity and Raman investigations on the phase transformations of $\text{Na}_4\text{P}_2\text{O}_7$, *J. Alloys Compd.* 340 (2002) 6.
- [96] S. Achigar, D. Caurant, E. Régnier, O. Majéus, Dismantling nuclear waste rich in P_2O_5 , MoO_3 and ZrO_2 : how do these oxides incorporate in aluminoborosilicate glasses? *J. Nucl. Mater.* 544 (2021), 152731.
- [97] A. Kaur, A. Khanna, A. Kaur, M.G.-B. Hirdesh, F. Gonzalez, Effects of annealing on density, glass transition temperature and structure of tellurite, silicate and borate glasses, *J. Non Cryst. Solids* 500 (2018) 443–452, <https://doi.org/10.1016/j.jnoncrysol.2018.08.035>.
- [98] J.E.K. Schawe, C. Wrana, Competition between structural relaxation and crystallization in the glass transition range of random copolymers, *Polymers (Basel)* 12 (8) (2020) 1778, <https://doi.org/10.3390/polym12081778>.
- [99] A. Buff, A Study of Crystallization Behaviour in Phase Separated Chalcogenide Glasses, Masters Thesis, University of Central Florida, 2016. <https://stars.library.ucf.edu/cgi/viewcontent.cgi?referer=&httpsredir=1&article=6140&context=etd> (accessed January 1, 2022).
- [100] T.C. Ong, T. Steinberg, E. Jaatinen, J. Bell, Suppression effects of cooling rate on crystallization in ZBLAN glass, *J. Non Cryst. Solids* 481 (2018) 306–313.
- [101] G.A. Sycheva, Nucleation and crystal growth in phase separated glasses in the lithium silicate system, in: E. Borisenko (Ed.), *Crystallization and Materials Science of Modern Artificial and Natural Crystals*, InTech, 2012.
- [102] S. Liu, Y. Zhang, Y. Yue, Effect of cooling rate on crystallization in an aluminophosphosilicate melt, *Phys. Chem. Glasses* 52 (2011) 6.
- [103] V.V. Akimov, Viscosity of sodium-borosilicate glasses in the range of glass transition, *Fizika I Khimya Stekla* 15 (6) (1989).
- [104] T. Yazawa, K. Kuraoka, W. Du, Effect of Cooling Rate on Pore Distribution in Quenched Sodium Borosilicate Glasses, *J. Phys. Chem. B* 103 (45) (1999) 9841–9845, <https://doi.org/10.1021/jp9923320>.
- [105] S. Peugot, E.A. Mauger, T. Charpentier, C. Mendoza, M. Moskura, T. Fares, O. Bouty, C. Jegou, *J. Non Cryst. Solids* 378 (2013) 201–212, <https://doi.org/10.1016/j.jnoncrysol.2013.07.019>.
- [106] D.-S. Kim, M.J. Schweiger, W.C. Buchmiller, J.D. Vienna, D.E. Day, D. Zhu, C.W. Kim, D.K. Peeler, T.B. Edwards, I.A. Reamer and R.J. Workman, Iron phosphate glass as an alternative waste-form for Hanford LAW, PNNL-14251, 15003646, (2003).
- [107] B.J. Riley, J.A. Rosario, and P.R. Hrma, Impact of HLW Glass Crystallinity on the PCT Response, PNNL-13491, 15001115, (2002).
- [108] I.W. Donald, *Waste Immobilization in Glass and Ceramic Based Hosts: Radioactive, Toxic and Hazardous Wastes*, John Wiley & Sons, 2010.
- [109] C. Rong, K.C. Wong-Moon, H. Li, P. Hrma, H. Cho, Solid-state NMR investigation of phosphorus in aluminoborosilicate glasses, *J. Non Cryst. Solids* 223 (1–2) (1998) 32–42, [https://doi.org/10.1016/S0022-3093\(97\)00436-5](https://doi.org/10.1016/S0022-3093(97)00436-5).
- [110] A.F. Craievich, E.E. Zanotto, P.F. James, Kinetics of sub-liquidus phase separation in silicate and borate glasses. A review, *Bulletin de Minéralogie* 106 (1983) 169–184, <https://doi.org/10.3406/bulmi.1983.7678>.
- [111] T.P. Seward, D.R. Uhlmann, D. Turnbull, Phase separation in the system BaO-SiO_2 , *J. Am. Ceram. Soc.* 51 (5) (1968) 278–285, <https://doi.org/10.1111/j.1151-2916.1968.tb13858.x>.
- [112] W. Deng, Y. Gong, J. Cheng, Liquid-phase separation and crystallization of high silicon canasite-based glass ceramic, *J. Non Cryst. Solids* 385 (2014) 47–54, <https://doi.org/10.1016/j.jnoncrysol.2013.11.006>.
- [113] D.R. Uhlmann, A.G. Kolbeck, Phase separation and the revolution in concept of glass structure, *Phys. Chem. Glasses* 17 (1976) 146–158.
- [114] X. Cheng, Phosphate-doped Borosilicate enamel Coating Used to Protect Reinforcing Steel from Corrosion, Doctoral Thesis, Missouri University, (2014). Accessed: Jan. 09, 2022. [Online].
- [115] V.P. Klyuev, Dependence of the dilatometric properties of glasses on their structure: I. Borate, aluminoborate, and lead-containing glasses, *Glass Phys. Chem.* 31 (2005) 749–759.
- [116] T. Minami, J.D. Mackenzie, Thermal expansion and chemical durability of phosphate glasses, *J. Am. Ceram. Soc.* 60 (1977) 232–235.
- [117] R.J. Kirkpatrick, R.K. Brow, Nuclear magnetic resonance investigation of the structures of phosphate and phosphate-containing glasses: a review. *Solid State Nuclear Magnetic Resonance, Solid State Nucl. Magn. Reson.* 5 (1) (1995) 9–21.
- [118] N. Keyvani, V.K. Marghussian, H.R. Rezaie, M. Kord, Effect of Al_2O_3 content on crystallization behavior, microstructure, and mechanical properties of $\text{SiO}_2\text{-Al}_2\text{O}_3\text{-CaO-MgO}$ glass-ceramics: effect of Al_2O_3 content on $\text{SiO}_2\text{-Al}_2\text{O}_3\text{-CaO-MgO}$ glass-ceramics, *Int. J. Appl. Ceram. Technol.* 8 (2011) 203–213.
- [119] X. Cheng, R.K. Brow, G. Chen, The dissolution behavior in alkaline solutions of a Borosilicate glass with and without P_2O_5 , *J. Am. Ceram. Soc.* 100 (2017) 4519–4532.
- [120] M.I. Ojovan, Viscosity and glass transition in amorphous oxides. *Advances in Condensed Matter Physics, 2008*, <https://doi.org/10.1155/2008/817829>.
- [121] P. Hrma, A.A. Kruger, High-temperature viscosity of many component glass melts, *J. Non Cryst. Solids* 437 (2016) 17–25, <https://doi.org/10.1016/j.jnoncrysol.2016.01.007>.
- [122] A.L. Sadler, A new viscosity model for waste glass formulations, Conference 98: annual meeting of the American Ceramic Society, Indianapolis, United States (1996).
- [123] J.C. Mauro, Y. Yue, A.J. Ellison, P.K. Gupta, D.C. Allan, Viscosity of glass-forming liquids, *Proc. Natl. Acad. Sci. U.S.A.* 106 (47) (2009), <https://doi.org/10.1073/pnas.0911705106>.
- [124] F. He, C. Ping, Y. Zheng, Viscosity and structure of lithium sodium borosilicate glasses, *Phys. Procedia* 48 (2013) 73–80, <https://doi.org/10.1016/j.phpro.2013.07.012>.
- [125] Z. Zhang, H. Zhang, Y. Yang, The rheology and morphology of phase-separating fluids with viscosity contrast, *J. Chem. Phys.* 115 (2001) 7783–7792.
- [126] J. Trimble, C. Brennan, A. Kovalskiy, Structural characterisation of tin fluorophosphate glasses doped with Er_2O_3 , *Phys. Chem. Glasses* 57 (2016) 27–31.
- [127] O.N. Koroleva, L.A. Shabunina, V.N. Bykov, Structure of borosilicate glass according to Raman spectroscopy data, *Glass Ceram.* 67 (2011) 340–342.
- [128] K. Litasov, N. Podgornykh, Raman Spectroscopy of Various Phosphate Minerals and Occurrence of Tuite in the Elga IIE Iron Meteorite: Raman Spectroscopy of Various Phosphate Minerals, *J. Raman. Spectrosc.* 48 (11) (2017) 1518–1527.